HHS Public Access

Author manuscript

Cell Rep. Author manuscript; available in PMC 2021 October 12.

Published in final edited form as:

Cell Rep. 2021 September 21; 36(12): 109733. doi:10.1016/j.celrep.2021.109733.

A long-range, recurrent neuronal network linking the emotion regions with the somatic motor cortex

Yihan Wang[1,2], **Qian-Quan Sun**[1,2,3,4,*]

[1]Graduate Neuroscience Program, University of Wyoming, Laramie, WY 82071, USA

[2]Department of Zoology and Physiology, University of Wyoming, Laramie, WY 82071, USA

[3]Wyoming Sensory Biology Center of Biomedical Research Excellence, University of Wyoming, Laramie, WY 82071, USA

[4]Lead contact

SUMMARY

Recurrent neural networks (RNNs) are designed to learn sequential patterns *in silico*, but it is unclear whether and how an RNN forms in the *native* networks of the mammalian brain. Here, we report an innate RNN, which is formed by the unidirectional connections from three basic units: input units arriving from emotion regions, a hidden unit in the medial prefrontal cortex (mPFC), and output units located at the somatic motor cortex (sMO). Specifically, the neurons from basal lateral amygdala (BLA) and the insular cortex (IC) project to the mPFC motor-cortex-projecting (MP) neurons. These MP neurons form a local self-feedback loop and target major projecting neurons of the sMO. Within the sMO, the neurons in the infragranular layers receive stronger input than the neurons in supragranular layers. Finally, we show *in vivo* evidence that the communications from the emotion regions to the sMO are abolished when MP neurons are chemogenetically silenced.

Graphical Abstract

*Correspondence: neuron@uwyo.edu.

AUTHOR CONTRIBUTIONS

Q.-Q.S. developed the concept and designed the experiments. Y.W. designed and performed the experiments, collected the data, and analyzed the data. Y.W. and Q.-Q.S. wrote the manuscript.

SUPPLEMENTAL INFORMATION

Supplemental information can be found online at https://doi.org/10.1016/j.celrep.2021.109733.

DECLARATION OF INTERESTS

The authors declare no competing interests.

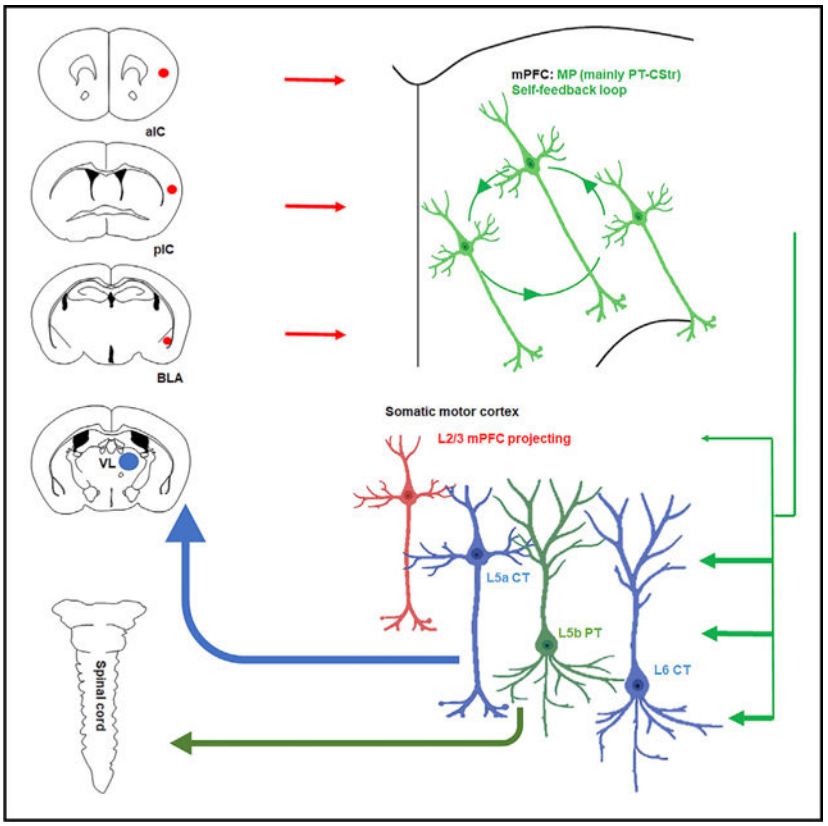

In brief

Wang and Sun show that the unidirectional, recurrent neuronal network, linking with the emotion regions and the somatic motor cortex, is formed by three basic units: input units arriving from the emotion regions, a hidden unit composed of self-feedback connected medial prefrontal cortex (mPFC) neurons, and output units located at the somatic motor cortex (sMO).

INTRODUCTION

The artificial recurrent neural network (RNN) has been extensively applied in the fields of language learning, sequential auto-association, and robotic control (Medsker and Jain, 1999). It is a neural network with self-feedback (closed loop) connections (Fausett, 1994). Specifically, the RNN consists of three conceptual units, including an input unit, a hidden unit, and an output unit. The key features of the RNN include the following: (1) the connection among three units is unidirectional (input → hidden → output), and (2) the self-feedback connections are formed within the hidden unit. Recent studies highlight the important roles of the recurrent circuit on amplification (Peron et al., 2020) and feedback inhibition (Bolding and Franks, 2018) *in vivo*. Self-feedback connections were delineated in local motor, visual, and frontal cortices (Brown and Hestrin, 2009; Kiritani et al., 2012; Morishima and Kawaguchi, 2006). However, whether these self-feedback connections contribute to the functional RNN, which is composed of three conceptual units and two key features, is unclear.

The same projecting neurons, or the neurons in the same cortical layers, share similar transcriptomes in certain brain regions (Economo et al., 2018; Lui et al., 2021; Tasic et al., 2018). They can be arranged into the same unit, which corresponds to an artificial unit. Thus, the connectivity of neurons within a same projecting or laminar group can be thought as self-feedback connectivity. In the motor cortex, the self-feedback connectivity of the intratelencephalic (IT) neurons is high, but they also recurrently connect with corticothalamic (CT) neurons (Yamawaki and Shepherd, 2015). In the prefrontal cortex, pyramidal-tract (PT) corticopontine (Cpn) neurons overlap with CT neurons in layer (L) 5 and have greater positive self-feedback connectivity than IT-corticostriatal (CStr) neurons (Collins et al., 2018; Morishima and Kawaguchi, 2006). However, there is a reciprocal connection between the prefrontal cortex and the thalamus (Collins et al., 2018). In the visual cortex, inputs from the thalamus target recurrent L4 neurons, which further innervate L2/3 neurons (Morgenstern et al., 2016). However, thalamic inputs also innervate L2/3 neurons directly. Therefore, none of the above reported connectivity can meet the criterion of the RNN architecture.

Here, we show a long-range neuronal network, which can be described as an innate RNN. It is formed with a self-feedback connectivity in the medial prefrontal cortex (mPFC; the hidden unit), which integrates inputs from basal lateral amygdala (BLA) and insular cortex (IC) neurons (the input units) and further innervates the somatic motor cortex (sMO) infragranular-layer-projecting neurons (the output units). We first demonstrate that the laminar and region-specific distribution of motor-cortex-projecting (MP) neurons in the mPFC, where L5 MP neurons receive stronger input from the BLA than from its L2/3 counterparts. We, then, show that, in the mPFC, the L5 MP neurons are PT-CStr neurons, whereas the L2/3 counterparts are cortico-cortical (CC) neurons, which project to the motor cortex. The connections from the BLA and ICs to the MP neurons are unidirectional. Within the mPFC, the MP neurons highly innervate CStr, but not CT- or BLA-projecting neurons, forming a relatively isolated, local self-feedback loop. Next, we found that MP neurons preferentially innervate the sMO-infragranular-layer-projecting neurons (CT and PT-CSpi), which do not project to the mPFC. Given the role of CT and PT-CSpi neurons on movement preparation and execution (Economo et al., 2018; Maier et al., 2002; Ueno et al., 2018), this suggests that the function of this circuit is related to voluntary movement control. Moreover, BLA and IC share similar projection patterns. Finally, we illustrate that chemogenetic silencing of the key component of this RNN MP neuron abolishes *trans*-synaptic communication from the emotion regions (BLA and ICs) to the sMO. Our results also indicate that the MP subtype—the PT-CStr neurons—have a key role in this network.

RESULTS

The L5 MP neuron in the mPFC mediates the connection between the BLA and the motor cortex

The mPFC has been reported to connect the BLA and motor cortex (Little and Carter, 2013; Muñoz-Castañeda et al., 2020;Ährlund-Richter et al., 2019). It is, thus, a possible region that mediates connections between the BLA and the motor cortex. To confirm that connection and to identify the higher-order regions of the mPFC and the relevant neurons

that mediate it, we used red adeno-associated virus (AAV-retrograde [retro]) (Tervo et al., 2016) to label CC neurons from contralateral mPFC, green AAV-retro to label MP neurons from ipsilateral primary motor cortex (M1); and Fluoro-Gold to label CT neurons from the ipsilateral thalamus (in the mediodorsal [MD] and ventromedial [VM] regions of the thalamus) (Figure 1A, box 1). We confirmed the connection BLA → mPFC and mPFC → M1 by analyzing the distribution of mPFC-projecting neurons and MP neurons, respectively (Figures S1A and S1B). We, then, examined the distribution of MP neurons in two different regions of the mPFC (Figures 1B and 1C). In the dorsal (d) mPFC, 32% ± 4% MP neurons were in L2/3, and 57% ± 3% of them were in L5 (Figures 1D and 1G). In the ventral (v) mPFC, 84% ± 11% MP neurons were in L5, whereas no more than 10% (one-sample t test) of them were observed in other layers (Figures 1D and 1E). Moreover, no more than 5% (one-sample t test) of the MP neurons co-localized with the CC (contralateral mPFC projection) or CT neurons (Figures 1F and 1G).

Our anatomy data showed that MP neurons are mainly distributed in L2/3 and L5 of the dmPFC and in L5 of the vmPFC. We, thus, investigated the BLA synaptic inputs to the dmPFC L2/3 and L5 MP neurons and the vmPFC L5 MP neurons. We injected AAV-channelrhodopsin-2 (ChR2) into the ipsilateral BLA, to label the BLA axons, and AAV-retro into the M1, to label MP neurons (Figure 1A, bottom), followed by performing whole-cell patch-clamp recordings from the MP neurons and other pyramids using subcellular ChR2-assisted circuit mapping (sCRACM) (Petreanu et al., 2009; Figures 1A and 1H–1K). The input strength of the BLA → L5 MP neurons was, on average, 12.5 times stronger than that of the L2/3 counterparts in the dmPFC (Figure 1J), whereas there was no significant difference between the L5 MP and other L5 pyramids in either the vmPFC or the dmPFC (Figures 1J and 1K). For both dmPFC and vmPFC L5 MP neurons, the BLA inputs were mainly targeted on soma proximal dendrites (Figures 1H and 1I). These findings demonstrate that L5, but not L2/3, MP neurons mainly mediate communications from the BLA to the motor cortex. In addition, the L5 MP neurons and other pyramids in the dmPFC and vmPFC share a similar BLA innervation preference.

We next examined whether there are any unique features of the L5 MP neurons that could separate them from other L5 pyramids. Using the same injection approach as used for sCRACM (Figure 1A, box 2), we compared the intrinsic membrane properties and dendritic morphologies of L5 MP neurons versus other L5 pyramids (Figures 1l and S1C–S1F). As expected, we found that L5 MP neurons had significantly longer apical dendrites (Figures S1E and S1F), higher sag ratio values, and higher rheobase measurements (Figures S1C and S1D) than other L5 pyramids had. This allowed L5 MP neurons to be clustered into a distinct group from the other L5 pyramids (Figure 1L; group1, circle: 100% GFP-neurons versus group 2, square: 81% GFP+ neurons). However, dmPFC and vmPFC L5 pyramids were evenly distributed between the two groups (Figure 1L; group 1, circle: 4 vmPFC/8 dmPFC pyramids versus group 2, square:, 7 vmPFC/9 dmPFC pyramids). These data are consistent with a previous report (Lui et al., 2021), showing similar transcriptomic and spatial organization between the dmPFC and the vmPFC.

The cell types of the mPFC MP neuron and its local connectivity

The sag ratio of the membrane potential and dendritic length is also an indicator that distinguishes PT and IT neurons (Kawaguchi, 2017; Shepherd, 2013). To further identify the cell type of the MP neuron, we examined its genetic profile and projections (Figure 2). We had the advantage that PT, but not IT, neurons express chicken ovalbumin upstream of the promoter transcription factor-interacting protein 2 (Ctip2) (Arlotta et al., 2005). We separately injected AAV-retro into the thalamus to label the CT neurons (as a PT positive control) and AAV-retro into the motor cortex to label the MP neurons in different mice, followed by immunohistological labeling of Ctip2 (Figure 2A). We observed a strong overlap of CT (79% ± 3%) and L5 MP (72% ± 5%) neurons with $Ctip2^+$ neurons, whereas poor co-localization (14% ± 8%) was found in L2/3 (Figures 2A and 2B). These findings indicate that L5 and L2/3 MP neuron are genetically distinct cell types; of which, the L5 MP neuron is mainly the PT type, whereas the L2/3 counterpart is mainly the IT type. Given that the L2/3 IT neuron has only CC projections (Shepherd, 2013), these L2/3 MP neurons are mainly CC (motor cortex projection) neurons.

To define the cell type of the MP neuron by its projection, we injected the plasmid pENN-cre (Zingg et al., 2017; Zingg et al., 2020) into the BLA, followed by the Cre-dependent AAV-flex into the ipsilateral mPFC to label the projections of the BLA connected to the mPFC neurons (as positive control) and AAV-retro-cre into the motor cortex, followed by Cre-dependent AAV-flex into the ipsilateral mPFC to label the projections of the MP neurons, in separate mice (Figure 2C). We defined the sMO through an AAV-retro subpial injection into the spinal cord (Tadokoro et al., 2017) and employed landmark-based registration of the brain slices to a common coordinate framework (Figure S2A; STAR Methods). Axon length was measured through neurite reconstruction (Winnubst et al., 2019; Figure S2B; STAR Methods). Among mapped brain regions, we found that BLA-connected mPFC neurons were densely projected to the ipsilateral thalamus, ipsilateral sMO, ipsilateral caudate putamen (Cpu), the ipsilateral BLA, the contralateral mPFC, and the contralateral Cpu (Figures 2C–2F). By contrast, the MP projections to the thalamus and BLA were insignificant (Figures 2C and 2D; no more than 5% of all measured regions, one-sample t test) and were low to the contralateral Cpu (Figure 2D; MP projections to the contralateral Cpu/to the ipsilateral Cpu = 20% versus BLA-connected mPFC projections to the contralateral Cpu/to the ipsilateral Cpu = 79%). Moreover, the ventral part of the contralateral mPFC had few projections from the MP neuron (Figures 2E and 2F; 6% ± 2% of the entire contralateral mPFC projections), suggesting that vmPFC MP neurons do not have projections on the contralateral cortex. In addition, both projections of the MP neuron → BLA and the MP neuron → ICs were negligible (Figures S2C and S2D; no more than 5% of all measured MP projections, one-sample t test), suggesting that both the BLA → MP and ICs → MP neuron connection are unidirectional. Combined with our genetic profile results (Figures 2A and 2B), the clustering of the electrophysiological parameters (Figure 1L), and the fact that the PT neuron has a higher sag ratio than IT neuron has, the IT neuron projects to the contralateral Cpu and contralateral cortex, and the CStr neuron projects to ipsilateral and contralateral Cpu (Kawaguchi, 2017; Shepherd, 2013), our findings indicate that dmPFC MP neurons consist of CC (in L2/3) and PT-CStr (in L5) neurons, whereas vmPFC MP neurons are mainly PT-CStr (in L5) neurons.

To study the local circuit of the MP neuron in the mPFC, we measured the synaptic strength of MP → CStr neurons, MP → CT neurons, and MP → BLA projecting neurons by performing sCRACM (Figure 3). MP neurons were infected with AAV-retro-ChR2-mcherry from a motor cortex injection, whereas CStr- and CT- or BLA-projecting neuron were labeled by injecting AAV-retro-GFP for the ipsilateral Cpu and Fluoro-Gold for the thalamus or BLA (Figure 3A). Our results showed that synaptic inputs from the MP neuron to the CStr neuron were, on average, 25 times and 10 times stronger than those to the CT neuron and the BLA-projecting neuron, respectively (Figure 3C). Given both the high connection probability of IT → PT and CStr → CStr (Brown and Hestrin, 2009; Morishima and Kawaguchi, 2006) and our finding that MP neurons are mainly composed of CC and PT-CStr neurons, the PT-CStr of the MP neurons mainly contribute to this local connectivity compared with the CC of MP neurons.

The long-range neuronal connectivity from the mPFC to the sMO

The sMO consists of PT-CSpi, CT, and groups of L2/3 neurons, which modulate voluntary movement (Lemon, 2008; Levy et al., 2020). To understand how these neurons connect to the mPFC, we labeled PT-CSpi, CT, and mPFC-projecting neurons by injecting AAV-retro-GFP, Fluoro-Gold, and AAV-retro-mcherry into spinal cord (in T13 and L1), the thalamus (in the VL), and the mPFC, respectively (Figure 4A, box 1). The mPFC injection site was designed according to anterogradely labeled axons from the motor cortex injection (Figure S3A). The distribution of mPFC-projecting neurons was analyzed across the entire sMO along the antero-posterior axis and the midline proximal-distal axis (Figure S4A) as well as the laminar depth (Figures 4B–4D). We found that 70% ± 6% mPFC-projecting neurons were located at L2/3, compared with 18% ± 5% in L5 and 12% ± 2% in L6 of the sMO (Figure 4D). We, thus, examined the intrinsic membrane properties of L2/3 mPFC-projecting neurons. They had lower spike frequency, higher spike heights, and lower resting membrane potential (RMP) than other sMO L2/3 pyramids (Figures S4B–S4D). Using these three electrophysiological parameters, 85% (11/13) of sMO L2/3 mPFC-projecting neurons were grouped into a distinct cluster versus the other sMO L2/3 pyramids (Figure 4E). Our results reveal that only a group of electrophysiologically distinct neurons, mainly located at the sMO L2/3, project to the mPFC.

As shown by the cell-type analysis, both CC and PT-CStr neurons in the dmPFC project to the sMO, whereas only PT-CStr neurons in the vmPFC project to the sMO (Figure 2). To distinguish the neuronal-specific input strength and laminar-specific input targets of PT-CStr and CC neurons on the sMO, we separately injected AAV-ChR2 into the dmPFC and vmPFC in different mice, and whole-cell recordings were made from tracer-labeled sMO-projecting neurons (Figure 4A, box 2). We first compared synaptic input strength in various types of projecting pyramids on the sMO. For comparison of the L5a CT, L5b PT-CSpi, L6 CT, and L2/3 mPFC-projecting neurons, we normalized synaptic strength in different types of neurons to that in the L5 CT neuron. For the L2/3 non-mPFC-projecting neuron, we compared the input strength to that of the L2/3 mPFC-projecting neuron. We found that the dmPFC and vmPFC to sMO inputs shared similar preferential patterns (Figures 4G and 4H). The input strength of both the dmPFC and vmPFC MP neurons → sMO depended on the cortical depth of the postsynaptic neurons. Inputs to supragranular

layer neurons (L2/3) were weaker than those of the infragranular layer neurons (L5/6) (Figures 4G and 4H). In the supragranular layer, the mPFC-projecting neurons received stronger inputs than other neurons did (Figures 4G and 4H). In the infragranular layer, the difference in input strength among the L5a CT, the L5b PT-CSpi, and the L6 CT was not significant (Figures 4G and 4H). These results suggest that the CT and PT-CSpi neurons of the sMO are the functional output (Cossell et al., 2015) of the MP neurons of the mPFC. We next compared the subcellular input targets between dmPFC → sMO and vmPFC → sMO. We found that dmPFC and vmPFC input peaks onto the L2/3 pyramids were a similar distance above the soma (Figures 5B and 5C; dmPFC, 96 μm ± 13 μm; vmPFC, 91 μm ± 10 μm). By contrast, the locations of dmPFC input peaks on the L5 and L6 pyramids were significantly different from that of vmPFC input peaks on those pyramids (dmPFC on L5: 92 μm ± 7 μm above soma, on L6: 62 μm ± 8 μm above soma versus vmPFC on L5: 43 μm ± 5 μm from soma, on L6: 13 μm ± 4 μm from soma) (Figures 5B and 5C). That suggests that the apical dendritic portion of the subcellular input target of dmPFC → sMO projections on L5 and L6 pyramids are largely mediated by the L2/3 CC neuron in the dmPFC.

Trans-synaptic projections from the BLA and ICs to the sMO

To better understand how BLA innervates the sMO via the mPFC, we injected pENN-Cre into the BLA, followed by Cre-dependent AAV-flex-ChR2 into the mPFC, to map the unidirectional *trans*-synaptic projecting target by sCRACM (Figures 5A–5C). Our results showed that the subcellular input target of BLA → mPFC → sMO pyramids was the same as that of the vmPFC → sMO pyramids but was different from that of the dmPFC → sMO pyramids (Figures 5B and 5C). In addition, the innervation preferences among dmPFC → sMO, vmPFC → sMO, and BLA → mPFC → sMO were similar (Figures 4G, 4H, and S5C). Because the PT-CStr neuron is the only neuronal type of MP neuron in the vmPFC (Figure 2), our results suggest it is a PT-CStr neuron, rather than a CC neuron, which mediates this *trans*-synaptic innervation. Indeed, the input strength of the BLA → CC neuron was, on average, 8% as strong as that of BLA → PT-CStr neuron (Figures 1J and 2).

Next, we asked whether the PT-CStr neuron also mediates the *trans*-synaptic projections of ICs → mPFC → sMO. These projections were anatomically confirmed by registration and axonal reconstruction in the sMO (Figure S5D). We compared the axonal distributions among neurons of dmPFC, vmPFC, BLA → mPFC, aIC → mPFC, and pIC → mPFC. To visualize these axons and clearly distinguish their locations, we minimally injected AAV-Venus into dmPFC and AAV-mcherry into vmPFC to label the dmPFC axon (green) and the vmPFC axon (red), respectively (Figure 5D). In the slice of Bregma −0.49 mm, the axonal fluorescent peak of vmPFC (957 ± 12 μm from midline) was closer to the midline than that of dmPFC (mean, 1,653 ± 35 μm from midline) (Figures 5D and 5F). The regional borders of the dmPFC and vmPFC axonal fluorescent peaks were delineated by the thresholds of the curves (Figure 5E). There was no significant difference between their vertical profiles of the slices of Bregma −0.94 mm (Figures S6B and S6C). To investigate the similarity of the BLA and IC *trans*-synaptic axonal distributions, we injected pENN-Cre into BLA, pIC, and aIC in three mice, followed by Cre-dependent AAV-flex-ChR2 into the mPFC, to label the BLA, pIC, and aIC *trans*-neuronal axons (Figures 5G–5I). We aligned their horizontal profiles to that of the dmPFC and vmPFC. Our results showed that all fluorescent

peaks of the BLA and IC trans-neuronal axons were located at the region of the vmPFC axonal fluorescent peak (Figures 5G–5I), implying that these axons are from the same type of neuron. Combined with the results of the cell-type identification that only L2/3 CC and L5 PT-CStr neurons in the mPFC project to the sMO (Figure 2), our findings suggest that PT-CStr neurons mediate communication from the BLA and IC to the sMO.

The necessity of the MP neuron for communication from the emotion regions to the sMO

To investigate the necessity of the MP neuron that mediates the transmission from the BLA and IC to sMO, we performed chemogenetic inhibition to inactivate the MP neuron and measured the electricity-evoked local field potential (LFP) of the sMO (Figure 6). The LFP largely reflects the excitatory synaptic current (Haider et al., 2016). It is, thus, an ideal measurement *in vivo* to match the sCRACM data *in vitro*. The pharmacologically selective actuator module (PSAM) is a useful chemogenetic tool, in which effects are mediated by ion channels (Magnus et al., 2019). Its ability to inhibit LFP and synaptic current was validated *in vivo* and *in vitro*, respectively, and the time course of the effect of the pharmacologically selective actuator module (PSAM) agonist (varenicline) was evaluated *in vivo* (Figure S7). We injected AAV-retro-cre into the motor cortex, followed by AAV-flex-PSAM into the mPFC to label t he MP neurons and inactivated these labeled MP neurons by varenicline administration (Figure 6A). We recorded sMO LFPs evoked by electrical stimulation on the BLA and ICs in freely moving mice (Figure 6B). Our results showed that administration of varenicline dramatically decreased the evoked LFPs in the sMO by BLA (mean, 85% decreases), aIC (mean, 87% decreases), and pIC (mean, 80% decreases) stimulation (Figures 6C and 6D). After 20 h of recovery, the evoked LPF amplitudes were rescued to nearly the values that were recorded during the pre-administration period (Figures 6C and 6D; BLA, mean, 78% rescue; aIC, mean, 77% rescue; pIC, mean, 107% rescue). Along with our results that PT-CStr neurons have the major functional role among these MP neurons (Figures 1, 2, and 5), this suggests that the PT-CStr neuron is necessary for mediation of the BLA and IC to the sMO in *trans*-synaptic communications.

A simple model of the innate RNN

Our results indicate that MP neurons (mainly PT-CStr) receive signals from the emotion regions and form a recurrent excitatory loop among themselves, transmitting the signal to the sMO (Figure 7A). We, therefore, proposed a model of RNN, which could process sequential movement efficiently in a robot (Zhou et al., 2020). In our RNN model, upstream neurons of BLA and ICs were arranged into the input units; MP neurons (mainly PT-CStr) were in the hidden unit; and downstream sMO infragranular layer projecting neurons (L5a CT, L5b PT-CSpi, and L6 CT) were in the output units (Figure 7A). After being unfolded with a timeline (Figure 7B), the hidden unit at time t received the input h_{t-1} happened at $t-1$, as well as the input x_t at time t. Thus, its output, h_t to the hidden unit in the next time state is given by Equation 1:

$$h_t = f\left(w^{hh}h_{t-1} + w^{hx}X_t\right) \quad \text{(Equation 1)}$$

where w^{hh} is the weight of the hidden unit to the hidden unit determined by the mPFC local inhibitory neurons; w^{hx} is the weight of the input unit to the hidden unit as determined by

the inhibitory neurons in the emotion regions. Its output, y_t to the output unit is given by Equation 2:

$$y_t = f\left(w^{hy}h_t\right) \quad \text{(Equation 2)}$$

where w^{hy} is the weight of the hidden unit to the output unit determined by sMO local inhibitory neurons. The model suggests that this innate RNN could process sequential movement by temporarily storing information and amplifying the emotional signal in mice, similar to what an artificial RNN does in a robot.

DISCUSSION

Our work identified an innate, long-range RNN that links the emotion regions to the sMO. We also provided detailed cellular and synaptic properties of each RNN component. For the hidden unit of this RNN, we showed that the mPFC MP neurons form a recurrent local circuit but have few local projections to other types of neurons (Figures 3B and 3C). Among the input units, hidden units, and output units, the connection is predominantly unidirectional from the input units to the output units, except for mPFC-projecting neurons in the sMO (Figures 2C, 2D, S2C–S2E, and S3B).

Technical considerations

In this study, our tracing method is based on the various AAV-retro and neuro-tracers and Fluoro-Gold. These genetic and chemical tracers have different infecting properties, which could label different neurons in the upstream brain regions. Here, we discuss that possibility.

In the mPFC, we used two different AAV-retro tracers to label MP neurons. They all had similar laminar distribution profiles (Figures 1B, 1C, and S3B). We also performed a control experiment (Figure S1G) to demonstrate that. The results showed that both GFP- and mcherry-expressed neurons have similar membrane properties, suggesting that two cohorts of AAV-retro-labeled MP neurons belong to the same functional group in this mPFC → motor cortex pathway. For the mPFC CT neuron, we labeled it by using Fluoro-Gold; its laminar distribution profile is similar to that of the AAV-retro tracer (Collins et al., 2018; Figures 1B–1E), which suggests that Fluoro-Gold-labeled mPFC CT neuron is representative.

In the motor cortex, we visualized the CT neuron with Fluoro-Gold. It largely distributes in the L6, whereas the AAV-retro-labeled CT neurons mainly locate at L5a (Economo et al., 2018; Yamawaki and Shepherd, 2015). However, that does not affect our conclusion that the infragranular-layer neurons receive stronger input from the mPFC than the supragranular layer neurons in sMO receive because the input strength to the L5a CT resembles that of the L6 CT neurons (Figures 4G and 4H). For the motor cortex PT-CSpi neuron, we labeled it by injecting AAV-retro-GFP into the spinal cord. Positively labeled neurons were distributed exclusively in L5b (Figures 4B and 4C). This result is consistent with the literature showing that regardless of the viral or traditional tracing method, all labeled PT-CSpi neurons were in L5b (Anderson et al., 2010; Jara et al., 2016). Therefore, for this pathway, the issue of tracer variation does not arise. We labeled the motor cortex mPFC-projecting neurons with

AAV-retro-GFP or -mcherry. To prove they labeled the same type of neuron in the motor cortex, we preformed control experiments (Figure S4E). Even though only some of them (44% GFP-expressed neurons and 55% mcherry-expressed neurons) co-localized with each other, those neurons, which exclusively expressed GFP or mcherry, have similar membrane properties. Therefore, different AAV-retro tracing does not cause labeling of different types of neurons in this motor cortex → mPFC pathway.

Local connectivity of MP neurons in the mPFC

Our results showed that MP neurons in the mPFC consist of L2/3 CC neurons and L5 PT-CStr neurons (Figures 1B–1G, 2A, and 2B). Because L2/3 MP neurons receive weak innervation from BLA (Figure 1J), the PT-CStr neuron is the main functional subtype of MP neuron in our RNN model. All these MP neurons have a few local projections to other types of neurons, including CT- and BLA-projecting neurons (Figures 3B and 3C). Previous report has shown the unidirectional IT→ PT connectivity in the mPFC (Morishima and Kawaguchi, 2006), suggesting that PT-CStr neurons have no projection to local IT neurons either. In addition, the mPFC PT Cpn neuron overlaps with the CT neuron (Collins et al., 2018). Combined with the results showing that MP neuron weakly innervates the local CT neuron (Figure 3C), this suggests that the PT-CStr neuron also weakly innervates the local PT-Cpn neuron. Therefore, this PT-CStr loop in the mPFC may have no monosynaptic projection to the other types of local pyramidal neurons.

The functional implications

We demonstrated that MP neurons in the mPFC project only to motor regions, including the sMO and the caudate putamen (Figure S2E) and preferentially innervate the sMO infragranular layer, which regulates voluntary movement pyramids, including CT and PT-CSpi neurons (Asante and Martin, 2013; Economo et al., 2018; Maier et al., 2002; Ueno et al., 2018; Figures 4G and 4H). Among these MP neurons, PT-CStr neurons are the major functional group. We suggest that the main function of these PT-CStr neurons is motor control. Because PT-CStr neurons are widely distributed among various cortical regions, it is possible that PT-CStr neurons in other cortices have similar wiring diagrams as the have in the mPFC. Therefore, this innate RNN may provide a perspective on the computations of voluntary movement.

Although the CStr neuron was reported to drive decision making in the auditory cortex (Znamenskiy and Zador, 2013), the specific function of its subtypes, the IT-CStr and PT-CStr neurons, has not been distinguished in that earlier study. Indeed, the IT and PT neurons have distinct functions in motor learning and controlling processes. Specifically, the L2/3 pyramids (an IT type) report motor performance, whereas the L5 PT pyramids relate to movement and record memory traces of previous outcomes (Levy et al., 2020). One of the RNN function is to memorize the outcome of previous inputs. It suggests that the memorial function of the L5 PT pyramids may come from its CStr subtype and its networks within the innate RNN.

IC is an emotion-processing center and contains the primary interoceptive cortices (Craig, 2009; Craig et al., 2000). Stimulation of the IC can induce facial expressions (Dolensek et

al., 2020). Fear and anxiety are processed in the BLA (Lee et al., 2017). Stimulation of the BLA → mPFC increases freezing behavior (Burgos-Robles et al., 2017). We showed that the mPFC integrates inputs from both the BLA and ICs and that PT-CStr neurons in the mPFC have an important role in relaying these inputs to the sMO. Thus, direct inhibition of PT-CStr neurons may diminish the ability to emotionally regulate voluntary movement.

One of limitations of artificial RNNs is the vanishing gradient, which is suboptimal for processing long sequences. Thus, its corresponding, mammalian, innate RNN may also lack long-term memory-storage capability. Consequently, it may not be involved in modulating complex sequential movements. Indeed, visual stimulation affects eye movements only briefly (DeAngelus and Pelz, 2009).

Although we have demonstrated the circuit mechanism linking emotion and motor neurons, detailed movement patterns influenced by different emotional states and corresponding neuronal firings in each RNN unit have not been measured. Exploring these correlated neuronal firing patterns could shed lights on more-specific roles of the neuronal circuit under certain emotion states, such as control over certain voluntary patterns. In addition to the long-range excitatory circuit, knowledge about the local connectivity features linking PT-CStr neurons with different types of interneurons will be required to fully understand this innate RNN composition.

STAR★METHODS

RESOURCE AVAILABILITY

Lead contact—Further information and requests for resources and reagents should be directed to and will be fulfilled by the lead contact, Qian-Quan Sun (neuron@uwyo.edu).

Materials availability—This study did not generate new materials.

Data and code availability—Data availability. Data reported in this paper will be shared by the lead contact (neuron@uwyo.edu) upon request.

Code availability. All original code (clustering) has been deposited at Github and is publicly available as of the date of publication.

DOIs are listed in the Key resources table. sCRACM analysis code is provided by Dr. Hooks (mac.hooks@gmail.com).

Any additional information required to reanalyze the data reported in this paper is available from the lead contact (neuron@uwyo.edu) upon request.

EXPERIMENTAL MODEL AND SUJECT DETAILS

All experimental procedures were approved by the Institutional Animal Care and Use Committee (IACUC) and the Biosafety Committee of the University of Wyoming. All Immune-competent mice were bred on a C57/BL6J background. Postnatally (P) 12–90 days wild-type and CamKII-Cre mice were used for different purposes, and the specific ages were indicated in Method details. Mice older than P30 were housed with same sex littermate in

a vivarium maintained at 21–23°C on a 12 hr light/dark cycle. Male and female mice were used, no significant differences were found between these two groups.

Summary of mice used: For the anatomical and electrophysiological analysis of M1 projecting (MP) neuron, total 20 mice were used for this purpose (5 for anatomical analysis, 9 for sCRACM analysis, and 6 for current clamp; Figures 1 and S1). Some acquired slices from sCRACM and current clamp experiments were also used for imaging. Total 12 mice were used for immunohistology and axon length measurement (Figures 2 and S2). For local circuit mapping, total 3 mice were used for this purpose (Figure 3). 34 mice in total were used for mPFC to sM1 circuits mapping, anatomical analysis, and current clamp recordings (7 for anatomical analysis, 7 for sCRACM of dmPFC to sM1, 15 for sCRACM of vmPFC to sM1, and 5 for current clamp; Figures 4, 5, and S3–S6). In some experiments, sCRACM slices were also used for imaging. For dmPFC and vmPFC axon analysis, total 3 mice were used (Figures 5D, 5E, and S6). *Trans*-synaptic circuits mapping of BLA to sM1 used 6 mice (Figures 5B, 5C, and S5C). 3 mice were used for BLA and IC *trans*-synaptic axons analysis (Figures 5G–5I and S5D). LFP recording used 10 mice (WT and CamKII-Cre) in total (9 WT mice were used for inhibition testing of mPFC M1 projecting neurons and 1 CamKII-Cre mice were used for mPFC inhibition testing; Figures 6 and S7). Mice with low expression level were excluded from the study and their numbers were not counted.

METHOD DETAILS

Stereotaxic injection—For brain injection, P12-P18 animals were anesthetized with 2% isoflurane (v/v) and maintained with 0.4 LPM oxygenated 2% isoflurane (v/v) during the surgery. The animals were head fixed with a stereotaxic device (NARISHIGE SG-4N) and maintained at 37°C using a heat pad (K&H no.1060). A small craniotomy was made over the injection site. The delivery glass filament (Drummond Scientific Co.) with around 5 μm tip diameters were backfilled with 20–300 nL virus or beads. Pressure injection using a customized device driven by single axis hydraulic manipulator (NARISHIGE mmo-220A) delivered virus or bead into the desired regions at a rate of 30 – 50 nL min^{-1}. For spinal cord subpial injection: P30-P35 animals were used. They were fixed in another apparatus (Item 51615, Stoelting Co.) following a skin incision at Th10-L3 vertebrae level. Th13-L1 spinal segments were cut, and the pia matter was then punctured using delivery glass filament (Drummound Scientific Co.). 2 μL viruses were bilaterally delivered at a rate of 500 nL min^{-1}. The coordinates were relative to Bregma (Antero-posterior A-P, Medio-lateral M-L, Dorso-ventral D-V) in mm. Anterograde or retrograde tracing using pAAV-CAG-hChR2(H134R)-mCherry, pAAV-CAG-flex-ChR2-tdTomato, AAV-flex-Arch-GFP, pACAGW-ChR2-Venus-AAV, pAAV-Ef1a-mCherry-IRES-Cre, pAAV-CAG-GFP, pAAV-hSyn-mcherry, pAAV-CAG-hChR2(H134R)-mCherry, and fluoro-gold injected into mPFC (A-P 1.35, M-L 0.2, D-V 0.2 0.5 0.8 1.5 2.25), dmPFC (A-P 1.35, M-L 0.2, D-V 0.2 0.5 0.8 at an angle of 30° from upright), vmPFC (A-P 1.35, M-L 0.2, D-V 2.25), Motor cortex (A-P −0.6, M-L 1.0, D-V 0.2 0.5 0.8), CPu (A-P −0.2, M-L 2.5, D-V 2.1), BLA (A-P −1.7, M-L 3.1, D-V 3.6), aIC (A-P 1.5, M-L 2.5, D-V 2.0), pIC (A-P −0.5, M-L 3.5, D-V 2.0), VL (A-P −1.0, M-L 1.0, D-V 3.0), MD (A-P −1.0, M-L 0.4, D-V 2.75), VM (A-P −1.0, M-L 0.9, D-V 3.75), spinal cord (Th 13 to L1) as described in the result. *Trans*-synaptic intersectional anterograde tracing using

pENN-AAV-hSyn-Cre injected into BLA, pIC, aIC combined with AAV-flex injection into mPFC (A-P 1.35, M-L 0.2, D-V 0.2 0.5 0.8 1.5 2.25). Chemogenetic inhibition using AAV-SYN-flex-PSAM4-GlyR-EGFP injected into mPFC combined with AAV-retro into motor cortex. Animal were returned to the home cage until at least 3 weeks before they were being used for experiments.

Slice preparation—Animals were anesthetized with 2% isoflurane (v/v) and intracardially perfused with an ice-cold cutting buffer (2.5 KCl, 1.25 NaH_2PO_4, 10.0 $MgCl_2$, 0.5 $CaCl_2$, 26.0 $NaHCO_3$, 11.0 glucose, and 234.0 sucrose in mM; bubbled with 95% O_2 and 5% CO_2). Angled coronal sections (15 ° downward with respect to the coronal plane) were cut in 300 μm thickness by a vibrating blade microtome (Leica VT1000s). Then, these slices were transferred to 34°C oxygenated (95% O_2 and 5% CO_2) ACSF (126.0 NaCl, 2.5 KCl, 1.25 NaH_2PO_4, 1.0 $MgCl_2$, 2.0 $CaCl_2$, 26.0 $NaHCO_3$ and 10.0 glucose in mM) for 1 hr. Recordings were performed at room temperature.

Patch clamp recordings—Targeted neurons were visualized by infrared-differential interference contrast under a 60 × 1.0NA water-immersion objective (Olympus). Layers were manually identified by the density of CT, PT-CSpi (sM1), and CC neurons under a 4 × 0.1NA objective (Olmpus) and the cell size under a 60 × 1.0NA water-immersion objective. Fluorescence was detected using a mercury short ARC (OSRAM). CT or BLA projecting neurons were identified by blue fluorescence of fluoro-gold retro beads. PT-CSpi and CC neurons were identified by green or red fluorescent protein expression in cell bodies. Patch pipettes were pulled with a P-97 puller (Sutter Instrument) generating a 4–5 MΩ resistance. In voltage-clamp experiments, pipettes were filled with a Cs-based biocytin-included (0.5%, wt/vol) intracellular solution (130 CS-gluconate, 10 phosphocreatine-Tris, 3 $MgCl_2$, 0.07 $CaCl_2$, 4 EGTA, 10 HEPES, 4 Na_2-ATP, and 1 Na-GTP in mM, pH 7.35 with CsOH 289 mOsm). In current-clamp experiments, pipettes were filled with a K-based biocytin-included (0.5%, wt/vol) intracellular solution (130 K-gluconate, 10 phosphocreatine-Tris, 3 $MgCl_2$, 0.07 $CaCl_2$, 4 EGTA, 10 HEPES, 4 Na_2-ATP, and 1 Na-GTP in mM, pH 7.35 with KOH 287 mOsm). For sCRACM, 1 μM TTX and 0.1 mM 4-AP were added into bath solution to block action potential and repolarize the axons, respectively. Data were collected with an Axopatch 700B amplifier (Axon Instruments) and a 1322A board. sCRACM data were collected using a MATLAB-based software Ephus (Suter et al., 2010). Sampling rate is at 10 kHz and holding potentials are around −65 mV for voltage clamp.

Photostimulation—A blue laser beam (Shanghai Laser & Optics Century Co., 473 nm) was controlled by routing mirrors, Pockels cell (ConOptics), and galvanometer scanners to deliver through a 4 × objective at the specimen plane. Each cell was mapped with a 12 × 18 photostimulation grid (distance between adjacent points, 75 μm), which was centered horizontally over the apical dendrite of the recorded cell. Each map was repeated 2–6 times and averaged. A pseudo-random photostimulation was given to avoid the interference between the stimulation of adjacent grid spots.

Histology—P30-P90 injected animals were anesthetized with 2% isoflurane (v/v) and perfused intracardially with 0.9% saline followed by 4% PFA. For the comparison of

axon fluorescence on motor cortex (Figures 5D–5F), only age P60-P80 female mice (C57 background only) were used to minimize the difference of the slices. Brains or spinal cords were extracted and stored in 4% PFA overnight at 4°C. Fixed brains or spinal cords were washed three times before dehydration in 30% sucrose for 24 hr. Slices were cut on a cryostat (MICROM, HM505E) at 70 μm thickness after embedding with an optimal cutting temperature compound (Tissue tek). For immune-blotting, the slices were blocked with 10% goat serum after washing three times by PBST (0.01 M PBS + 3% Triton X-100) and thereafter incubated with rat anti-Ctip2 (1:1000) for 48–70 hours or mouse anti-Cre (1:1000) for 36–48 hours at 4°C and Goat anti-rat (1:1000) or Goat anti-mouse (1:1000) for 2 hours at room temperature. Anti-fade mounting medium with or without DAPI (VECTASHIEID) was applied to mount slice. In the experiments of neuronal reconstruction, 300 μm recorded slices were fixed by 4% PFA overnight. After three times washing by PBST, slices were blocked by 2% BSA in PBST for 4 hr. Biotin filled neurons were stained by 1:100 AMCA Avidin D antibody for 24 hr at 4°C. Fluorescent images were acquired by an LSM 980 microscope. For the reconstruction of projections and recorded neurons, 20 × 0.8NA objective (Zeiss) was used. In other experiments, a 10 × 0.45NA objective (Zeiss) was used.

Surgical implantation of intracranial electrodes—Animals were used after viral injection at least 3 weeks. Bipolar twisted-metal electrodes (polyimide-insulated stainless-steel wire, 0.127 mm, California fine Wire Co.) were cut to a designed length and attached to a connecting pin (0.508 mm gold pin, Mill-Max Mfg. Corp.). They were implanted unilaterally into a small craniotomy over the implant site by a micromanipulator. For BLA implant, the electrodes were attached to a plastic fiber to avoid bending. For ground implant, a unipolar electrode was placed at olfactory bulb. The coordinates were relative to Bregma (Antero-posterior A-P, Medio-lateral M-L, Dorso-ventral D-V) in mm. Implant sites followed olfactory bulb (A-P 4.0, M-L 1.0, D-V 1.0 as reference), BLA (A-P −1.9, M-L 3.1, D-V 3.6), pIC (A-P −0.5, M-L 4.0, D-V 2.4), aIC (A-P 1.7, M-L 2.5, D-V 3.0), sM1 (A-P −1.0, M-L 1.0, D-V 0.8), vS1 (A-P −1.0, M-L 3.0, D-V 2.75). We used dental cement (Lang Dental) to secure the implanted electrodes.

LFP recordings—A piezo sensor was added at the bottom of the cage to detect the movements. LFP and floor-sensor signals were amplified using a differential AC amplifier (model 1700, A-M systems). Data were collected with an Axon Digidata 1322A board. The data on the sleeping state were used for analysis. Stimulation current was given by a digital stimulus isolation amplifier (Model BJN8-9V1, Getting Instruments) at the range of 0.1mA–1mA and the duration of 0.5 ms. Stimulation frequency was 0.246 Hz, which kept unchanged for each experiment. Signals were recorded with a 10 kHz sampling rate and were then low pass filtered from 40 Hz using Bessel to remove the influence of electrode cables.

Chemogenetic inhibition—For *in vitro* experiments, varenicline was added into the bath solution at 10 nM final concentration. Voltage-clamp recording was performed 2 min after administration. For *in vivo* experiments, injected animals were administered intraperitoneally with varenicline (3 mg kg^{-1}). LFP recording was performed 0.5 to 1.5 hours after administration.

Data analysis—For current-clamp recording, electrophysiological parameters were measured according to a previous study (Ma et al., 2006). Briefly, Fmax, steady state (Hz) was defined as the average frequency of the last three spikes, which measured at the maximal current step. Rin (MΩ) is input resistance, which was measured as the slope of the regression line of V – I curve. Spike height (mV) was measured as the difference between the peak action potential and the corresponding resting membrane potential. RMP (Resting Membrane Potential, mV) was measured after breaking the seal without current applied. Tau (membrane time constant, ms) was determined from the monoexponential curve (best fitting) at the current step +20 pA or −20 pA. Rheobase (pA) was determined as the intercept of the F steady state – I curve with the current axis. Sag ratio is the slope of the regression line of Sag – membrane potential curve. Sag was measured as the difference between the most negative and positive potential at the single hyperpolarizing current step. Collected electrophysiology parameters of each cell were clustered into two groups by K-means in an iterative manner (Figures 1L and 4E). t-SNE was used for dimensional reduction (Figure 4E).

For voltage-clamp recording, sCRACM data were analyzed using custom MATLAB scripts. In Ephus, each trace was a 400-ms recorded current (first 100 ms showed the baseline and the following 300 ms showed the evoked EPSC). The value of each map pixel corresponded to the EPSC charge in a 200-ms time window after the laser onset. For *in vitro* chemogenetic inhibition (Figure S7C), all pixels with synaptic responses were included. For other individual cell mapping, only the pixels over the threshold (> 3 × standard deviation of the baseline) were included. Other sCRACM cloud maps were computed using supra-threshold pixels and further averaged across cells within a class. Paired comparisons across cells used signed-rank test, comparing summed supra-threshold input of individual cells.

For quantitative analyses of cell number, an ImageJ plugin Cell Counter was used. The number of retrogradely labeled neurons in discrete brain cortices or regions was normalized to the maximal cell number of the counting areas and averaged across animals. Distance from midline was used to sort neurons into 400 μm bins (Figure S4A). Neurons in each bin were counted using above normalization method. For those neurons in the layers of certain brain cortices, the input or output number was normalized to the total number of detected neurons. 50 μm bins were used for sorting neurons (Figures 1D, 1E, and 4C). We divided layers through the threshold of CC and CT neurons' curves. For anatomical analysis of axons, captured images were decreased the resolution following gray value measurement. These gray values were normalized by the maximum and averaged across animals. For neurites tracing, we used simple neurites tracing (ImageJ) following Sholl analysis (Ferreira et al., 2014; Figure 5B). The nomenclature, abbreviation, and ontology were referred to the Mouse Brain Stereotaxic Coordinate (MBSC, Paxinos and Franklin, 2004; Table S2). The brain area border lines were aligned to the coronal diagram. sM1 definition and the corresponding border lines were coordinated to our labeled PT-CSpi neurons by spinal cord injection.

For axon length measurement (Winnubst et al., 2019), we used five features (Gaussian blur, Hessian, Sobel filter, Difference of Guassian, Membrane Projections) to train a classifier.

Two morphological features were included. Probability maps, of which each pixel reflects the likelihood of it belonging to axons, were then created. The skeleton maps were the centerline extraction of the probability maps after thresholding (Figures S2B and S5D). For those large pictures, we first divided them into small parts, detecting axons in each part. We then stitched them using pairwise stitching (Preibisch et al., 2009) without overlap (ImageJ).

The registration was based on point reference. In some experiments, the captured brain slices with spinal cord injection and with telencephalic injection were registered to the Common Coordinate Framework (CCF) at the corresponding coordinates (Figure S2A). In other experiments, the captured brain slices with spinal cord injection were registered to the captured brain slices with brain injection directly (Figure S5D). We manually selected a group of reference points in both CCF and captured brain slices. The captured brain slices were then transformed through bUnwarpJ (ImageJ). We merged Transformed brain slices into a single image. sM1 was thus defined by limiting to the area where PT-CSpi neurons distributed.

QUANTIFICATION AND STATISTICAL ANALYSIS

The exact number of used mice and recorded cells are described in the figures and figure captions. The statistical significance of the cell intrinsic properties (Figures S3C, S3D, and S4D), dendritic length comparisons (Figures S3E and S3F), fluorescence peak distances (Figures 5F and S6C), and amplitude peak comparisons was determined by two sample t test (Minitab) with a 95% confidence interval (Table S1), the significance input strength comparisons (Figures 1J, 1-K, 4G, and 4H) were performed by signed rank test (MATLAB), and the significance of cell density (Figures 1G and S1A) and axon lengths (Figures 2D and S2D) was performed by one sample t test (MATLAB). For two sample t test and signed rank test, we assumed that the difference between two groups is significant when the p value < 0.05. For one sample t test, we assumed that the value is significantly different from 0.1 or 0.05 when the p value < 0.05. Error bars were reported as arithmetic mean ± SEM.

Supplementary Material

Refer to Web version on PubMed Central for supplementary material.

ACKNOWLEDGMENTS

We thank Z. Zhang for imaging and C. Zhang for histology assistance. We thank K. Pratt and K. Mruk for discussion and comments. B. Hook provided MATLAB codes for the sCRACM analysis. This work was supported by grants from the National Institutes of Health (5R01NS094550, 1R21AG072803-01, 3P20GM121310-04S2, and P20GM121310 to Q.-Q.S.).

REFERENCES

Ährlund-Richter S, Xuan Y, van Lunteren JA, Kim H, Ortiz C, Pollak Dorocic I, Meletis K, and Carlén M (2019). A whole-brain atlas of monosynaptic input targeting four different cell types in the medial prefrontal cortex of the mouse. Nat. Neurosci 22, 657–668. [PubMed: 30886408]

Anderson CT, Sheets PL, Kiritani T, and Shepherd GM (2010). Sub-layer-specific microcircuits of corticospinal and corticostriatal neurons in motor cortex. Nat. Neurosci 13, 739–744. [PubMed: 20436481]

Arlotta P, Molyneaux BJ, Chen J, Inoue J, Kominami R, and Macklis JD (2005). Neuronal subtype-specific genes that control corticospinal motor neuron development in vivo. Neuron 45, 207–221. [PubMed: 15664173]

Asante CO, and Martin JH (2013). Differential joint-specific corticospinal tract projections within the cervical enlargement. PLoS ONE 8, e74454. [PubMed: 24058570]

Bolding KA, and Franks KM (2018). Recurrent cortical circuits implement concentration-invariant odor coding. Science 361, eaat6904. [PubMed: 30213885]

Brown SP, and Hestrin S (2009). Intracortical circuits of pyramidal neurons reflect their long-range axonal targets. Nature 457, 1133–1136. [PubMed: 19151698]

Burgos-Robles A, Kimchi EY, Izadmehr EM, Porzenheim MJ, Ramos-Guasp WA, Nieh EH, Felix-Ortiz AC, Namburi P, Leppla CA, Presbrey KN, et al. (2017). Amygdala inputs to prefrontal cortex guide behavior amid conflicting cues of reward and punishment. Nat. Neurosci 20, 824–835. [PubMed: 28436980]

Chow BY, Han X, Dobry AS, Qian X, Chuong AS, Li M, Henninger MA, Belfort GM, Lin Y, Monahan PE, and Boyden ES (2010). High-performance genetically targetable optical neural silencing by light-driven proton pumps. Nature 463, 98–102. [PubMed: 20054397]

Collins DP, Anastasiades PG, Marlin JJ, and Carter AG (2018). Reciprocal circuits linking the prefrontal cortex with dorsal and ventral thalamic nuclei. Neuron 98, 366–379.e4. [PubMed: 29628187]

Cossell L, Iacaruso MF, Muir DR, Houlton R, Sader EN, Ko H, Hofer SB, and Mrsic-Flogel TD (2015). Functional organization of excitatory synaptic strength in primary visual cortex. Nature 518, 399–403. [PubMed: 25652823]

Craig AD (2009). How do you feel–now? The anterior insula and human awareness. Nat. Rev. Neurosci 10, 59–70. [PubMed: 19096369]

Craig AD, Chen K, Bandy D, and Reiman EM (2000). Thermosensory activation of insular cortex. Nat. Neurosci 3, 184–190. [PubMed: 10649575]

DeAngelus M, and Pelz JB (2009). Top-down control of eye movements: Yarbus revisited. Vis. Cogn 17, 21.

Dolensek N, Gehrlach DA, Klein AS, and Gogolla N (2020). Facial expressions of emotion states and their neuronal correlates in mice. Science 368, 89–94. [PubMed: 32241948]

Economo MN, Viswanathan S, Tasic B, Bas E, Winnubst J, Menon V, Graybuck LT, Nguyen TN, Smith KA, Yao Z, et al. (2018). Distinct descending motor cortex pathways and their roles in movement. Nature 563, 79–84. [PubMed: 30382200]

Fausett L (1994). Fundamentals of Neural Networks: Architectures, Algorithms, and Applications (Prentice-Hall).

Fenno LE, Mattis J, Ramakrishnan C, Hyun M, Lee SY, He M, Tucciarone J, Selimbeyoglu A, Berndt A, Grosenick L, et al. (2014). Targeting cells with single vectors using multiple-feature Boolean logic. Nat. Methods 11, 763–772. [PubMed: 24908100]

Ferreira TA, Blackman AV, Oyrer J, Jayabal S, Chung AJ, Watt AJ, Sjöström PJ, and van Meyel DJ (2014). Neuronal morphometry directly from bitmap images. Nat. Methods 11, 982–984. [PubMed: 25264773]

Haider B, Schulz DP, Haüsser M, and Carandini M (2016). Millisecond coupling of local field potentials to synaptic currents in the awake visual cortex. Neuron 90, 35–42. [PubMed: 27021173]

Jara JH, Stanford MJ, Zhu Y, Tu M, Hauswirth WW, Bohn MC, DeVries SH, and Özdinler PH (2016). Healthy and diseased corticospinal motor neurons are selectively transduced upon direct AAV2–2 injection into the motor cortex. Gene Ther. 23, 272–282. [PubMed: 26704722]

Kawaguchi Y (2017). Pyramidal cell subtypes and their synaptic connections in layer 5 of rat frontal cortex. Cereb. Cortex 27, 5755–5771. [PubMed: 29028949]

Kiritani T, Wickersham IR, Seung HS, and Shepherd GM (2012). Hierarchical connectivity and connection-specific dynamics in the corticospinal-corticostriatal microcircuit in mouse motor cortex. J. Neurosci 32, 4992–5001. [PubMed: 22492054]

Lee SC, Amir A, Haufler D, and Pare D (2017). Differential recruitment of competing valence-related amygdala networks during anxiety. Neuron 96, 81–88.e5. [PubMed: 28957678]

Lemon RN (2008). Descending pathways in motor control. Annu. Rev. Neurosci 31, 195–218. [PubMed: 18558853]

Levy S, Lavzin M, Benisty H, Ghanayim A, Dubin U, Achvat S, Brosh Z, Aeed F, Mensh BD, Schiller Y, et al. (2020). Cell-type-specific outcome representation in the primary motor cortex. Neuron 107, 954–971.e9. [PubMed: 32589878]

Little JP, and Carter AG (2013). Synaptic mechanisms underlying strong reciprocal connectivity between the medial prefrontal cortex and basolateral amygdala. J. Neurosci 33, 15333–15342. [PubMed: 24068800]

Lui JH, Nguyen ND, Grutzner SM, Darmanis S, Peixoto D, Wagner MJ, Allen WE, Kebschull JM, Richman EB, Ren J, et al. (2021). Differential encoding in prefrontal cortex projection neuron classes across cognitive tasks. Cell 184, 489–506.e26. [PubMed: 33338423]

Ma Y, Hu H, Berrebi AS, Mathers PH, and Agmon A (2006). Distinct subtypes of somatostatin-containing neocortical interneurons revealed in transgenic mice. J. Neurosci 26, 5069–5082. [PubMed: 16687498]

Magnus CJ, Lee PH, Bonaventura J, Zemla R, Gomez JL, Ramirez MH, Hu X, Galvan A, Basu J, Michaelides M, and Sternson SM (2019). Ultrapotent chemogenetics for research and potential clinical applications. Science 364, eaav5282. [PubMed: 30872534]

Maier MA, Armand J, Kirkwood PA, Yang HW, Davis JN, and Lemon RN (2002). Differences in the corticospinal projection from primary motor cortex and supplementary motor area to macaque upper limb motoneurons: an anatomical and electrophysiological study. Cereb. Cortex 12, 281–296. [PubMed: 11839602]

Mao T, Kusefoglu D, Hooks BM, Huber D, Petreanu L, and Svoboda K (2011). Long-range neuronal circuits underlying the interaction between sensory and motor cortex. Neuron 72, 111–123. [PubMed: 21982373]

Medsker L, and Jain LC (1999). Recurrent Neural Networks: Design and Applications, First Edition (CRC Press).

Morgenstern NA, Bourg J, and Petreanu L (2016). Multilaminar networks of cortical neurons integrate common inputs from sensory thalamus. Nat. Neurosci 19, 1034–1040. [PubMed: 27376765]

Morishima M, and Kawaguchi Y (2006). Recurrent connection patterns of corticostriatal pyramidal cells in frontal cortex. J. Neurosci 26, 4394–4405. [PubMed: 16624959]

Muñoz-Castañeda R, Zingg B, Matho KS, Wang Q, Chen X, Foster NN, Narasimhan A, Li A, Hirokawa KE, Huo B, et al. (2020). Cellular anatomy of the mouse primary motor cortex. bioRxiv. 10.1101/2020.10.02.323154.

Paxinos G, and Franklin K (2004). Paxinos and Franklin's The Mouse Brain in Stereotaxic Coordinates, Fifth Edition (Academic).

Perez F, and Granger BE (2007). IPython: A System for Interactive Scientific Computing. Comput. Sci. Eng 9, 21–29.

Peron S, Pancholi R, Voelcker B, Wittenbach JD, Ólafsdóttir HF, Freeman J, and Svoboda K (2020). Recurrent interactions in local cortical circuits. Nature 579, 256–259. [PubMed: 32132709]

Petreanu L, Mao T, Sternson SM, and Svoboda K (2009). The subcellular organization of neocortical excitatory connections. Nature 457, 1142–1145. [PubMed: 19151697]

Preibisch S, Saalfeld S, and Tomancak P (2009). Globally optimal stitching of tiled 3D microscopic image acquisitions. Bioinformatics 25, 1463–1465. [PubMed: 19346324]

Shepherd GM (2013). Corticostriatal connectivity and its role in disease. Nat. Rev. Neurosci 14, 278–291. [PubMed: 23511908]

Suter BA, O'Connor T, Iyer V, Petreanu LT, Hooks BM, Kiritani T, Svoboda K, and Shepherd GM (2010). Ephus: multipurpose data acquisition software for neuroscience experiments. Front. Neural Circuits 4, 100. [PubMed: 21960959]

Tadokoro T, Miyanohara A, Navarro M, Kamizato K, Juhas S, Juhasova J, Marsala S, Platoshyn O, Curtis E, Gabel B, et al. (2017). Subpial adeno-associated virus 9 (AAV9) vector delivery in adult mice. J. Vis. Exp (125), 55770.

Tang JC, Drokhlyansky E, Etemad B, Rudolph S, Guo B, Wang S, Ellis EG, Li JZ, and Cepko CL (2016). Detection and manipulation of live anti-gen-expressing cells using conditionally stable nanobodies. eLife 5, e15312. [PubMed: 27205882]

Tasic B, Yao Z, Graybuck LT, Smith KA, Nguyen TN, Bertagnolli D, Goldy J, Garren E, Economo MN, Viswanathan S, et al. (2018). Shared and distinct transcriptomic cell types across neocortical areas. Nature 563, 72–78. [PubMed: 30382198]

Tervo DG, Hwang BY, Viswanathan S, Gaj T, Lavzin M, Ritola KD, Lindo S, Michael S, Kuleshova E, Ojala D, et al. (2016). A designer AAV variant permits efficient retrograde access to projection neurons. Neuron 92, 372–382. [PubMed: 27720486]

Ueno M, Nakamura Y, Li J, Gu Z, Niehaus J, Maezawa M, Crone SA, Goulding M, Baccei ML, and Yoshida Y (2018). Corticospinal circuits from the sensory and motor cortices differentially regulate skilled movements through distinct spinal interneurons. Cell Rep. 23, 1286–1300.e7. [PubMed: 29719245]

Winnubst J, Bas E, Ferreira TA, Wu Z, Economo MN, Edson P, Arthur BJ, Bruns C, Rokicki K, Schauder D, et al. (2019). Reconstruction of 1,000 projection neurons reveals new cell types and organization of long-range connectivity in the mouse brain. Cell 179, 268–281.e13. [PubMed: 31495573]

Yamawaki N, and Shepherd GM (2015). Synaptic circuit organization of motor corticothalamic neurons. J. Neurosci 35, 2293–2307. [PubMed: 25653383]

Zhou X, Xu Z, Li S, Wu H, Cheng T, and Lv X (2020). RNN based adaptive compliance control for robots with model uncertainties. In AI Based Robot Safe Learning and Control (Springer), pp. 39–61. 10.1007/978-981-15-5503-9_3%U.

Zingg B, Chou XL, Zhang ZG, Mesik L, Liang F, Tao HW, and Zhang LI (2017). AAV-mediated anterograde transsynaptic tagging: mapping corticocollicular input-defined neural pathways for defense behaviors. Neuron 93, 33–47. [PubMed: 27989459]

Zingg B, Peng B, Huang J, Tao HW, and Zhang LI (2020). Synaptic specificity and application of anterograde transsynaptic AAV for probing neural circuitry. J. Neurosci 40, 3250–3267. [PubMed: 32198185]

Znamenskiy P, and Zador AM (2013). Corticostriatal neurons in auditory cortex drive decisions during auditory discrimination. Nature 497, 482–485. [PubMed: 23636333]

Highlights

- mPFC MP neurons consist of L2/3 CC neurons and L5 PT-CStr neurons
- MP neurons form a local, monosynaptic self-feedback loop in the mPFC
- mPFC MP neurons are necessary for communication from emotion regions to the sMO
- MP-PT-CStr neurons are the functional subtype in contacting emotion regions with the sMO

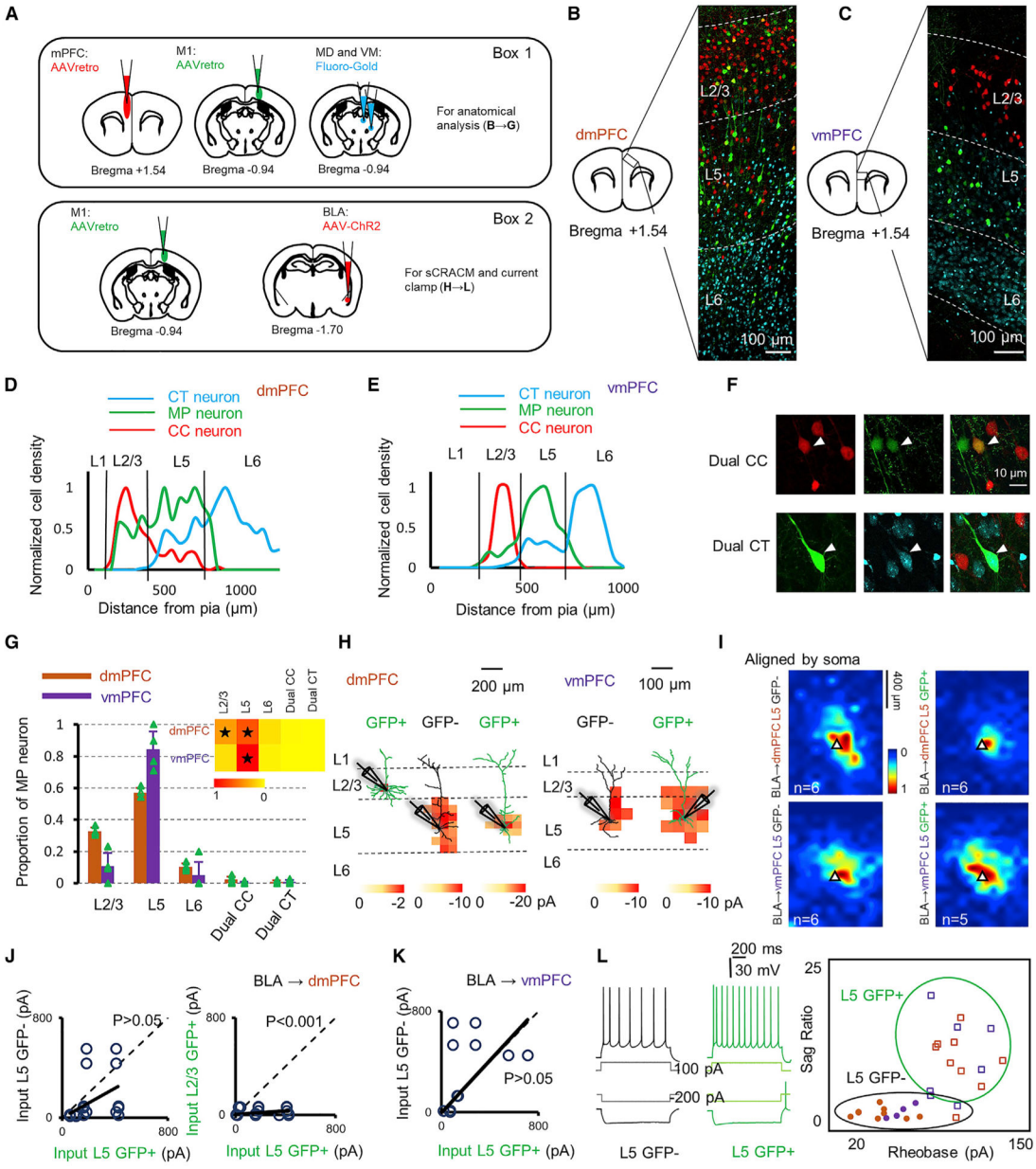

Figure 1. BLA input preferentially innervates L5 MP neurons in the mPFC

(A) The schematic shows the injection sites in the contralateral mPFC (red), ipsilateral M1 (green), medial dorsal (MD) and ventral medial (VM) thalamus (light blue), and the BLA (red). The corticocortical (CC) neurons, MP neurons, corticothalamic (CT) neurons, and BLA axons in the mPFC are labeled. As indicated, the injection approach was used for anatomical analysis (box 1), a different injection approach was used for sCRACM and the current clamp (box 2).

(B and C) Representative projection images show labeled neurons in the dmPFC (B) and vmPFC (C). Layers are divided by white dash lines according to cell size and the density of the CC neurons, which are mainly distributed in L2/3 as shown in (D) and (E), and CT

neurons, which are mainly distributed in L6 and partly in L5 as shown in (D) and (E). Red, CC neurons; green: MP neurons; cyan: CT neurons.

(D and E) The distribution of CC neurons, MP neurons, and CT neurons across the layers of dmPFC (D) and vmPFC (E). Layers are divided by black lines according to the threshold of the red and light blue curves.

(F) Representative images show dual CC neurons (CC neurons co-localized with MP neurons) and dual CT neurons (CT neurons co-localized with MP neurons).

(G) Summary of MP neuron distribution across layers and the proportion of dual CC and CT neurons in the dmPFC and vmPFC. Each green triangle represents one mouse. Inset: heatmap of the proportion of MP neurons. Values are arithmetic means ± SEM. Significant level *p = 0.1.

(H) Individual sCRACM input maps of MP neurons (GFP^+) and others (GFP^-) in dmPFC and vmPFC overlaid on reconstructions of the dendritic arbor.

(I) Averaged sCRACM maps aligned by soma (dmPFC: n = 5 mice; vmPFC: n = 4 mice).

(J and K) Comparison of input using L5 GFP^+ neurons as a reference. The inputs for L5 GFP^- (n = 14 pairs of cells, six mice), and for L2/3 GFP^+ (n = 18 pairs of cells, six mice) neurons in dmPFC are plotted (J), whereas, in the vmPFC, the inputs for L5 GFP^- (n = 13 pairs of cells, five mice) neurons are plotted (K). Statistics: signed-rank test. See also Table S1 for statistical values.

(L) The mPFC L5 neurons are categorized by the sag ratio and the rheobase (n = 11 for GFP^+ cells and n = 16 GFP^- cells in six mice). Left: individual raw traces of the recorded GFP^+ and GFP^- neurons in L5. Right: K-mean (K = 2) clustering of the recorded neurons. Categorized cells are coded for marker type (square and circle). Color represents the area in which the neurons are from (dmPFC: brown; vmPFC: purple). See also Figures S1C and S1D.

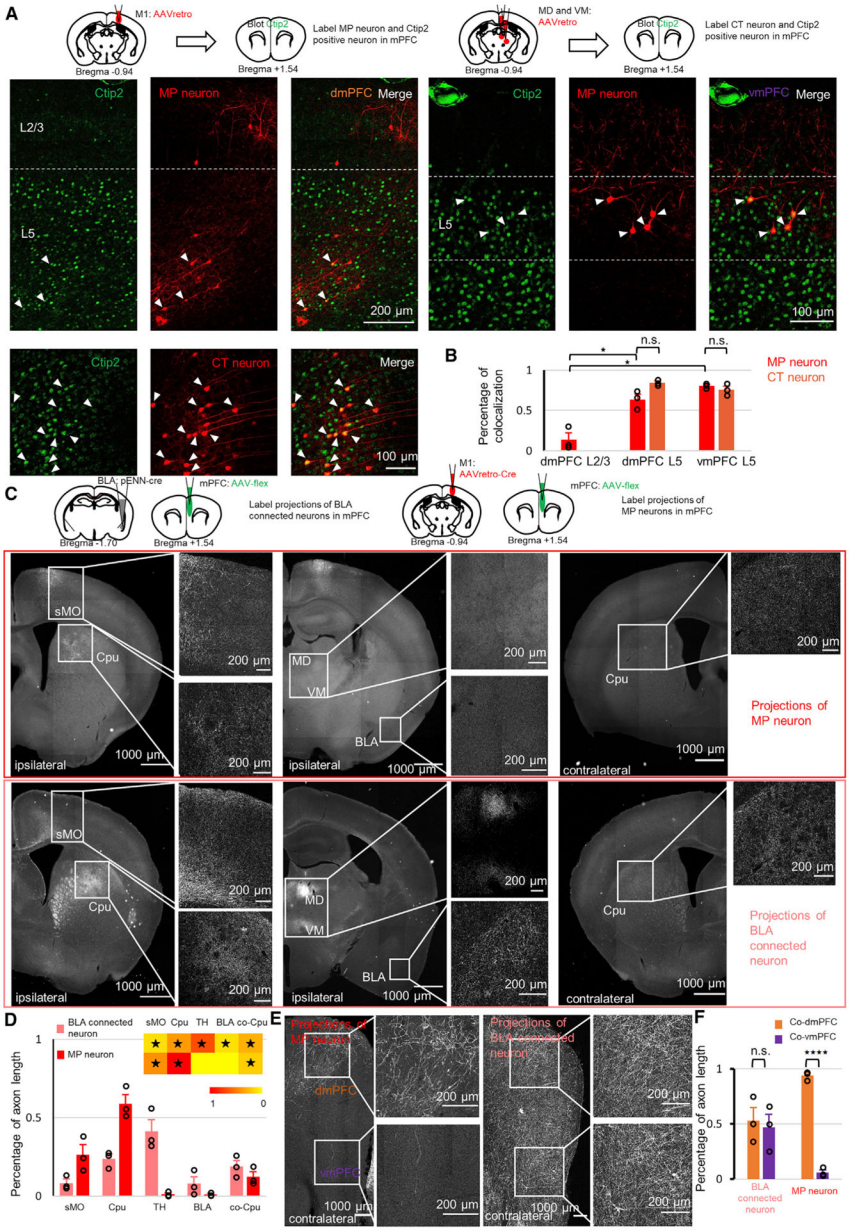

Figure 2. MP neurons in the mPFC send diverging projections to the caudate putamen and the motor cortex

(A) dmPFC and vmPFC L5 neurons co-localize with Ctip2$^+$ neurons. Top: injection schematic, with injection of AAV-retro into M1 (label MP neuron in the mPFC) and into MD/VM (label CT neuron in the mPFC). Bottom: representative images showing the co-localization (indicated by white arrow heads) of MP and CT neurons with Ctip2$^+$ neurons. Slice thickness: 70 μm.

(B) Percentages of labeled MP neurons and CT neurons co-localized with Ctip2$^+$ neurons in the dmPFC and vmPFC. Each circle represents one mouse. Values are arithmetic means ± SEM. *$p < 0.05$; n.s., not significant.

(C) Comparison of projections between mPFC BLA-connected neurons and MP neurons. Top: schematic images show injection sites in the BLA and mPFC (labeled projections

of mPFC neurons) and in M1 and mPFC (labeled projections of MP neurons). Bottom: representative images showing projection sites in the ipsilateral sMO, Cpu, MD, VM, BLA, and contralateral Cpu. Slice thickness: 70 μm.

(D) Summary of the distribution of mPFC BLA connected neurons' axons (pink) and mPFC MP neurons' axons (red). Each circle represents one mouse. Values are arithmetic mean ± SEM. Inset: the heatmap of the proportion of axon lengths. Significant level: *0.05. See also Figures S2A and S2B.

(E) Projections of mPFC BLA-connected neurons and MP neurons on the contralateral mPFC. Left two columns: representative images showing that MP neurons project only to the dorsal part of the contralateral mPFC. Right two columns: representative images showing that BLA-connected neurons project to both the dorsal and ventral part of the contralateral mPFC. Slice thickness: 70 μm. The slices were from the same mice shown in (C).

(F) Summary of the projections of mPFC BLA-connected neurons and MP neurons on the contralateral mPFC. Each circle represents one mouse. Values are arithmetic means ± SEM. n.s., not significant; ****$p < 0.0001$. See also Table S1 for statistical values. See also Figures S2C–S2E.

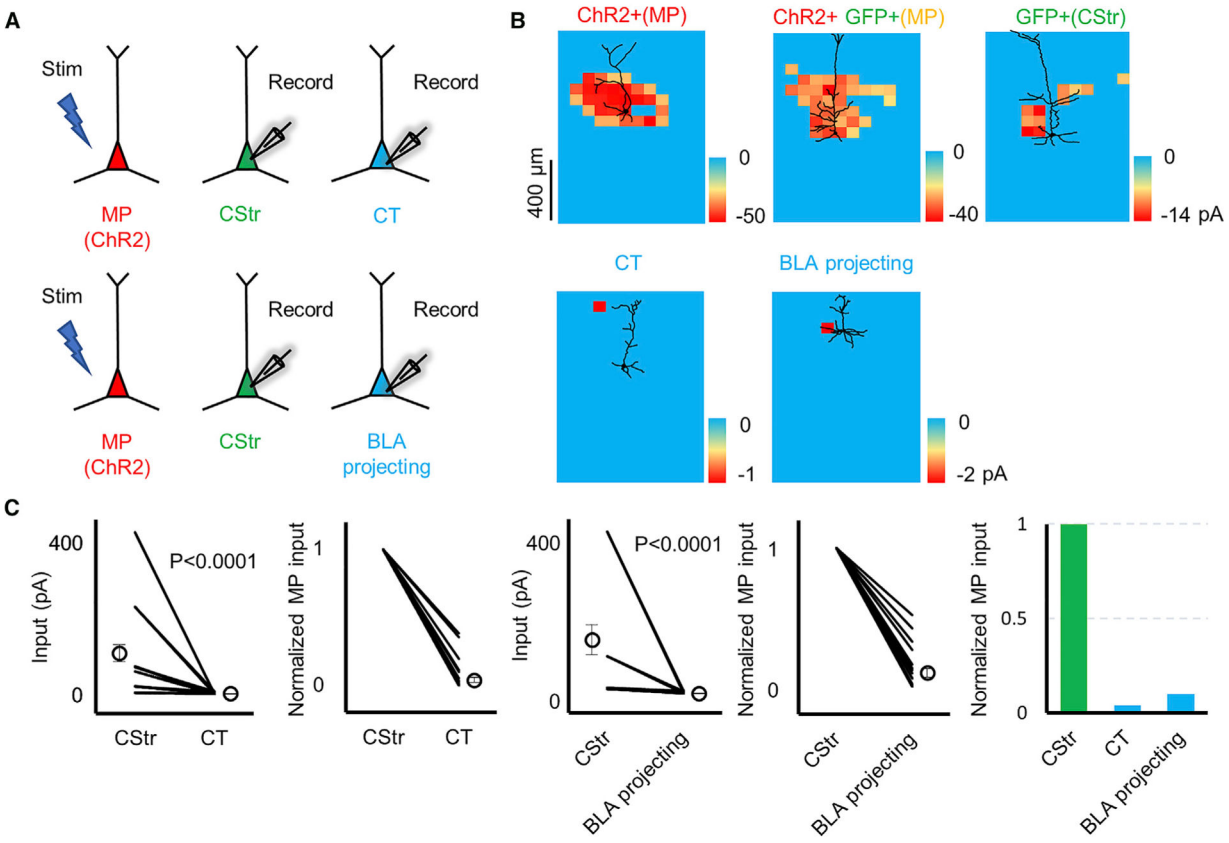

Figure 3. MP neurons preferentially innervate local CStr neurons in the mPFC

(A) Schematic of stimulation and recording configuration.

(B) Individual sCRACM input maps of MP neurons ($ChR2^+$ and ChR2-GFP double positive), CStr neurons (GFP^+), and CT- or BLA-projecting neurons (light blue) in the mPFC from MP neurons ($ChR2^+$) overlaid on reconstructions of the dendritic arbor.

(C) Comparison of input to CStr and CT neurons (n = 32 pairs of cells, three mice) or BLA-projecting neurons (n = 22 pairs of cells, two mice). Statistics: signed-rank test. The circles represent the mean (columns 1–4: 106 versus 1, 0.04; 138 versus 1, 0.1, from left to right). Black lines represent pairs of individual cells. Histogram chart (column 5, from left to right) describes the summary of comparisons. The bar heights are the values of corresponding circles in the columns 2 and 4 (from left to right).

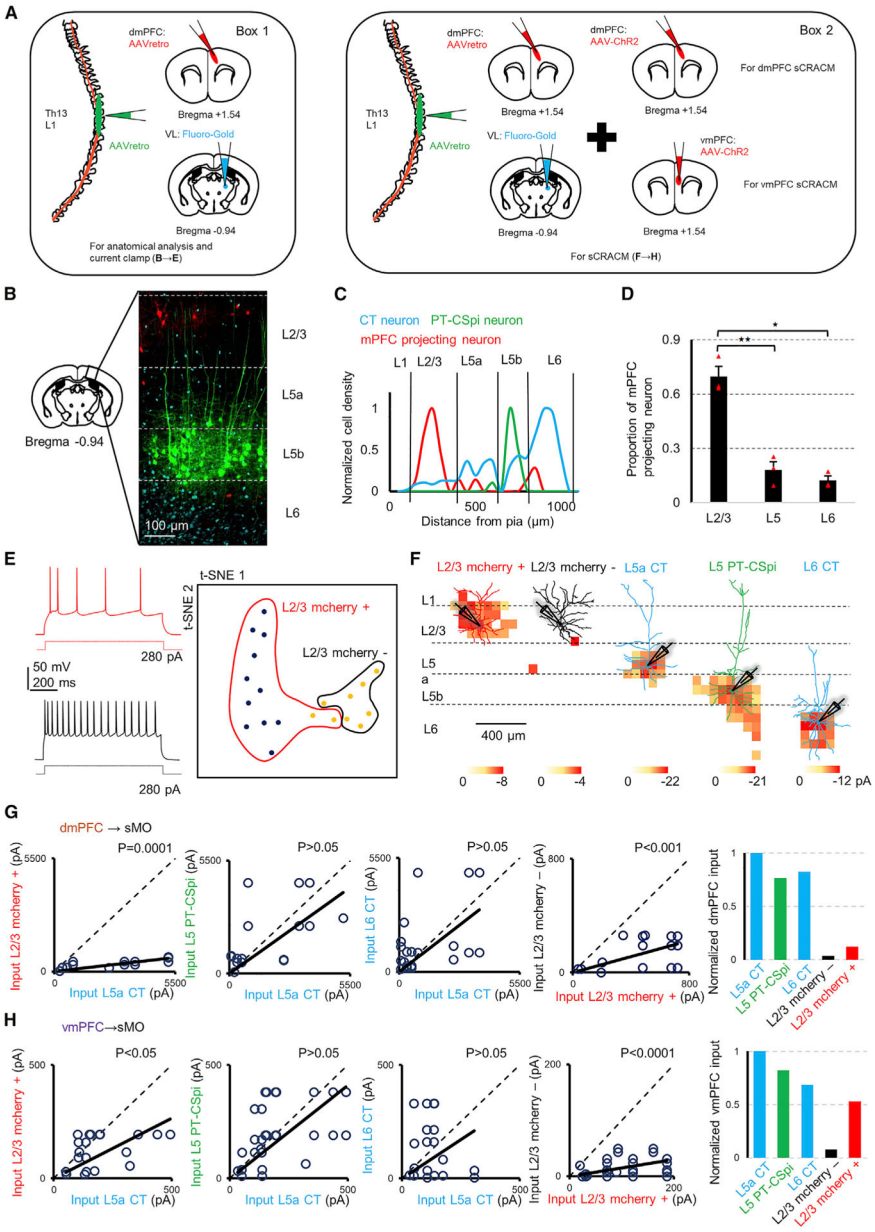

Figure 4. mPFC preferentially activate the neurons located at the infragranular layers of sMO

(A) Injection schematic images show injection sites in the dmPFC(red), spinal cord (green), ventral lateral (VL) thalamus (blue), and vmPFC(red). The labeled mPFC-projecting neurons or a mix of mPFC-projecting neurons and dmPFC axons, PT-CSpi neurons, CT neurons, and vmPFC axons are shown. As indicated, one injection approach was used for anatomical analysis and current clamp (box 1), whereas another was used for sCRACM (box 2). See also Figure S3 for the confirmation of dmPFC injection site.

(B) Projection images show labeled neurons and axons in the sMO. Left: schematic image indicates that the slice of Bregma at −0.94 mm was used for anatomic analysis. Right: representative image shows the labeled mPFC-projecting neuron (red), PT-CSpi neuron (green), and CT neuron (light blue). Layers are divided by white dashed lines according

to the density of the CT neurons (mainly distributed in L6 and partly in L5) and PT-CSpi neurons (mainly distributed in L5b) and cell size.

(C) The distribution of mPFC-projecting neurons, PT-CSpi neurons, and CT neurons across the layers of the sMO. Layers are divided by black lines according to the threshold of the red and light blue curves.

(D) Summary of the distribution of mPFC-projecting neurons across layers in the sMO. Values are means ± SEM. *$p < 0.05$, **$p < 0.01$. Each red triangle represents one mouse. See also Table S1 for statistical values.

(E) sMO mPFC-projecting neurons ($mcherry^+$) are categorized by amplitude peak, resting membrane potential (RMP), and maximum frequency in a steady state (FmaxSS). Left: individual raw traces of the recorded mcherry-positive and -negative neurons in L2/3. t-distributed stochastic neighbor embedding (t-SNE) was used for dimensional reduction, and K-means (K = 2) were used for clustering. Categorized cells are color-coded. The recording area was limited to the cortical column in which PT-CSpi neurons expressed. See also Figure S4.

(F) Individual sCRACM input maps of L2/3 mPFC-projecting neurons (red), other L2/3 neurons (black), and L5 CT neurons (light blue), L5 PT-CSpi neurons (green), and L6 CT neurons (light blue) in the sMO from vmPFC overlaid on reconstructions of the dendritic arbor. The recording area was limited to the cortical column in which PT-CSpi neurons are expressed. See also Figures S5A and S5B.

(G and H) Comparison of input using L5 CT neuron as the reference from the dmPFC (G) and vmPFC (H). Input for L2/3 mcherry positive (n = 14 pairs of cells, 5 mice) in (G) and (n = 20 pairs of cells, eight mice) in (H), for L5 PT-CSpi (n = 17 pairs of cells, six mice) in (G) and (n = 30 pairs of cells, eight mice) in (H), and for L6 CT (n = 20 pairs of cells, five mice) in (G) and (n = 19 pairs of cells, six mice) in (H) are plotted from columns 1–3 (from left to right), respectively. Comparison of input between L2/3 mcherry positive and negative cells (n = 18 pairs of cells, five mice) in (G) and (n = 26 pairs of cells, n = eight mice) in (H) are plotted in the column 4 (from left to right). Histogram chart (column 5, from left to right): summary of comparisons. The bar heights are the slopes of the regression lines in the left four columns (the bar height of L2/3 mcherry-negative cell = slope of column 1 × slope of column 4; the bar height of others = the slope of the corresponding charts). Statistics: signed-rank test. See also Table S1 for statistical values.

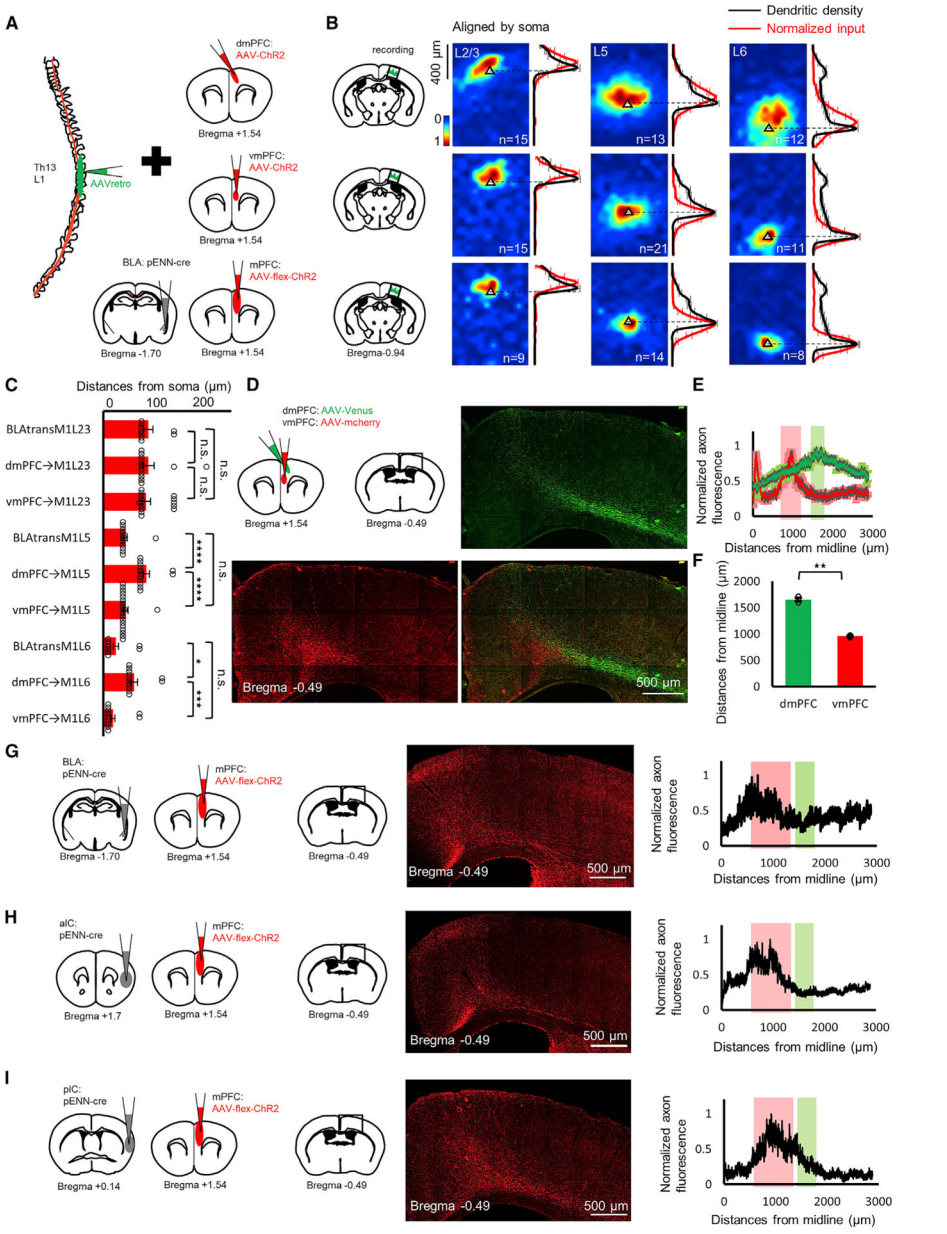

Figure 5. vmPFC, BLA, and ICs share similar mono-synaptic or *trans*-synaptic projection profile in the sMO

(A) Injection schematic depicts the injection sites of the dmPFC projection, vmPFC projection, and BLA *trans*-synaptically projection.

(B) Averaged sCRACM maps aligned by soma. Right: schematic images show the recording area was limited to the cortical column in which PT-CSpi neurons are expressed. Left: laminar input to sMO from dmPFC, from vmPFC, and *trans*-synaptically from BLA (from top to bottom, respectively). dmPFC and vmPFC → sMO input maps are from the same experiment as those in Figures 4G and 4H. Vertical profiles of normalized dendritic-length density and synaptic input were aligned by soma (cells used for dendritic reconstructions: L2/3, n = 15; L5, n = 15; L6, n = 14, five mice were used for mapping BLA *trans*-synaptic input). See also Figure S5C.

(C) Summary of the distances of input targets from the soma. Values are arithmetic means ± SEM. *p < 0.05, ***p < 0.001, ****p < 0.0001; n.s., not significant. Each circle represents one cell. See also Table S1 for statistical values.

(D) dmPFC (green) and vmPFC (red) projecting patterns on the cortex at Bregma −0.49 mm. Schematic images show injection sites and projection site. Representative magnified images of the area are shown in the black box.

(E) The distribution of dmPFC (green) and vmPFC (red) axon fluorescence along the x axis from the midline. Pink and light green colored backgrounds label the thresholds of the fluorescent intensity peak. See also Figure S6.

(F) Summary of the distances from fluorescent peaks to midline. Values are arithmetic means ± SEM. **p < 0.01. See Table S1 for statistical values.

(G–I). Axon distribution patterns on the cortex at Bregma −0.49 mm. Right: schematic images of injection sites and projection sites (black box). Middle: representative images showing the axon fluorescence distribution. Left: normalized axon fluorescent intensity along the x axis from the midline. Pink and light green colored backgrounds represent the thresholds of vmPFC and dmPFC axon fluorescent intensity peak, respectively.

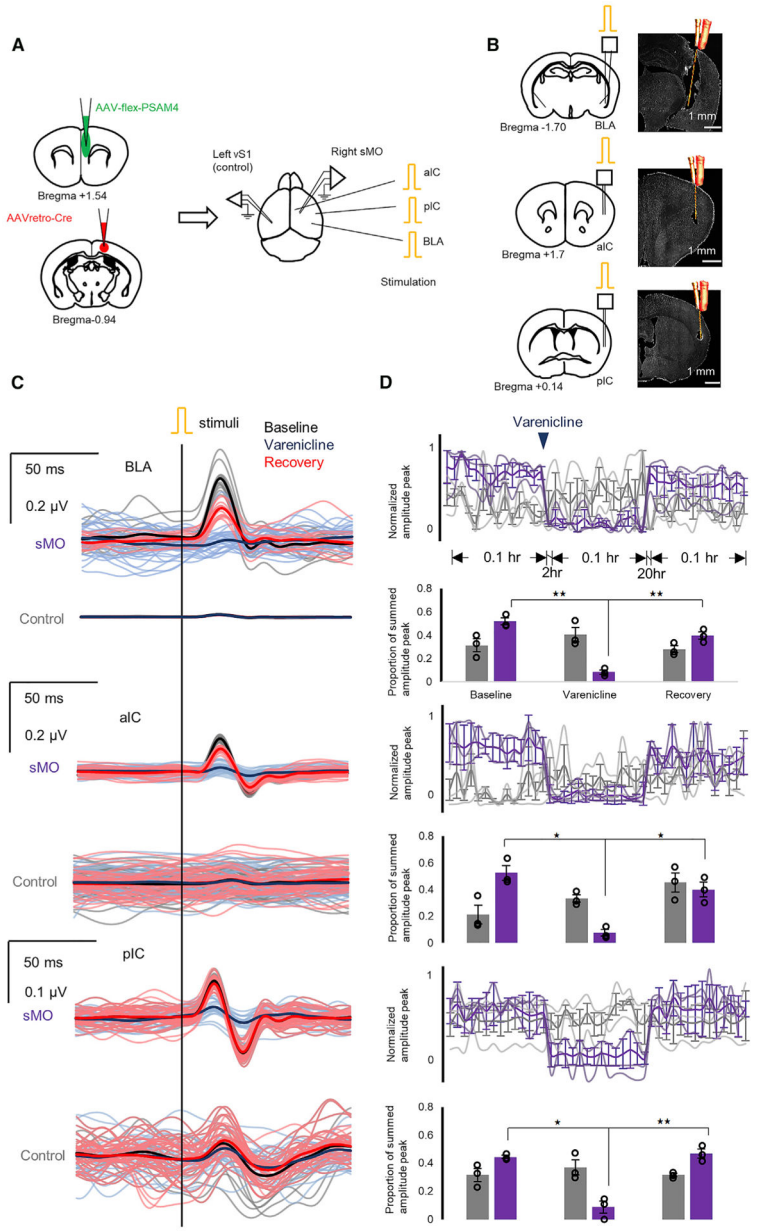

Figure 6. Inhibition of mPFC MP neurons eliminates the communication from BLA and ICs to the sMO

(A) Representative schematic shows injection and implant sites. Left: injection sites show PSAM is limited to expression in MP neurons in the mPFC. Right: recoding electrodes were implanted in the left vS1 (vibrissae primary sensory cortex) as a control and in the right sMO. Stimulating electrodes were implanted in the BLA, aIC, and pIC in three mice.

(B) Stimulation electrodes implant sites. Left: schematic images of implant sites. Right: representative images of implant sites.

(C) Local field-potential recordings in the sMO after electrical stimulation (5 ms; 0.246 Hz) on emotion regions (BlA, aIC, and pIC) before (black) and after (blue) 2 h of PSEM administration (3 mg kg^{-1}, intraperitoneally [i.p.]) and after 20 h of recovery (red). The solid trace is the average of the raw traces, which are plotted in shaded lines. See also Figure S7.

(D) The time course before and after PSEM administration. Each circle represents one mouse. Values are arithmetic means ± SEM. Statistic: *$p < 0.05$, **$p < 0.01$. See Table S1 for statistical values.

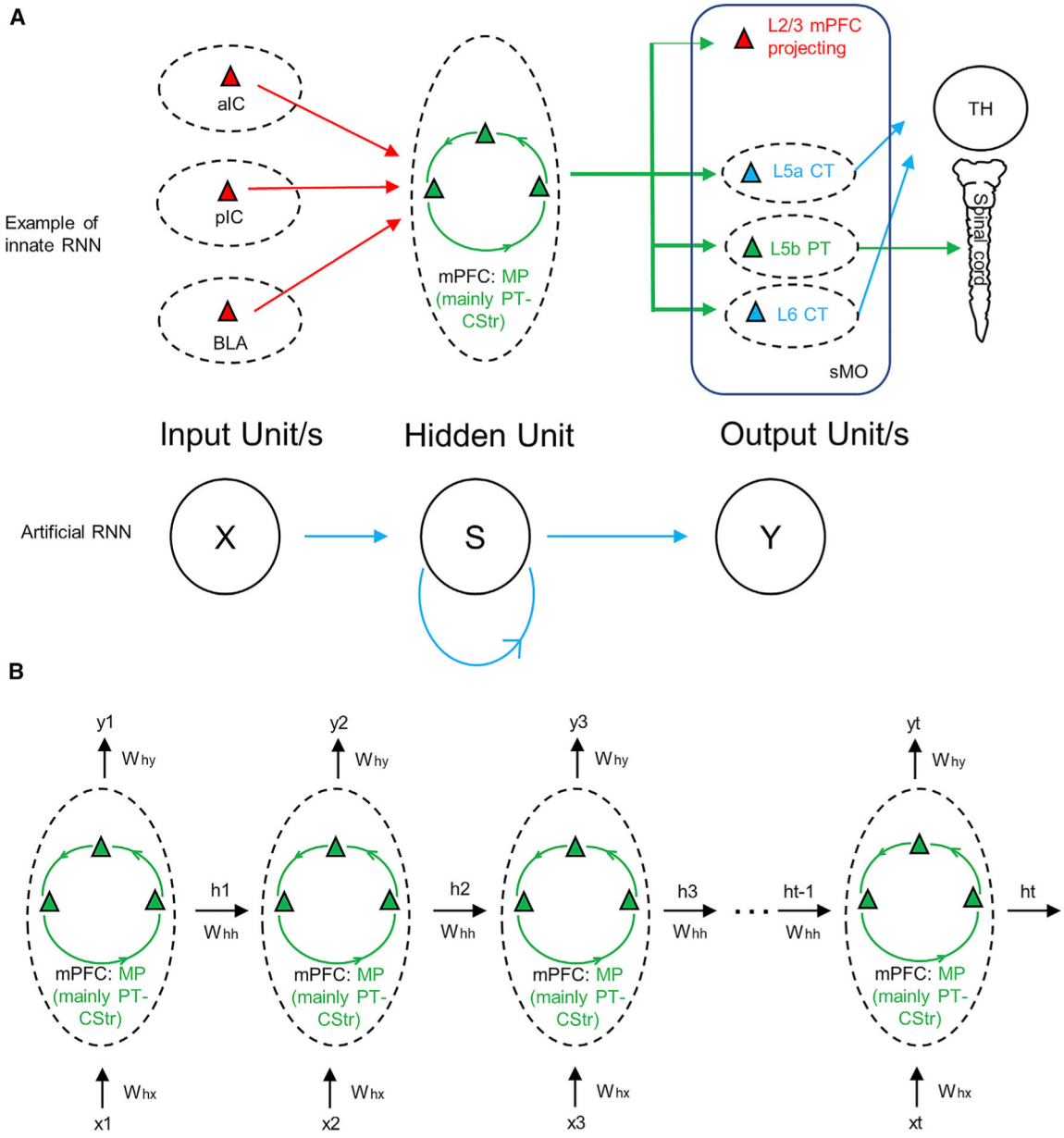

Figure 7. The RNN linking emotion regions with mPFC and sMO

(A) Top: the schematic image describes the neurons in the emotion regions (BLA, aIC, and pIC), which activate (red arrow) the MP (mainly PT-CStr) neurons in the mPFC. Excited MP neurons magnify the signal by activating themselves. They further transmit the signal to the downstream sMO neurons (thick green arrow representing strong innervation, whereas the thin green arrow means a weak input). In the sMO, excited L5a CT neurons and L6 CT neuron further connect (blue arrow) the TH (thalamus); excited L5b PT-CSpi neurons innervate (green arrow) the spinal cord. Each dashed circle represents one unit. Bottom: simple model of artificial RNN.

(B) A model of an innate RNN unfolded by timeline. x, input; y, output; w, weight; h, hidden.

KEY RESOURCES TABLE

REAGENT or RESOURCE	SOURCE	IDENTIFIER
Antibodies		
Rat anti-Ctip2	Abcam	RRID: AB_2064130
Mouse anti-Cre	Milipore	RRID: AB_2085748
Goat anti-rat	Jackson ImmunoResearch	RRID: AB_2338308
Goat anti-mouse	ThermoFisher	RRID: AB_2534062
AMCA Avidin D antibody	Vector Laboratories	RRID: AB_2336102
Bacterial and virus strains		
pAAV-CAG-hChR2(H134R)-mCherry	Unpublished data	pAAV.CAG.hChR2(H134R)-mCherry.WPRE.SV40 was a gift from Karl Deisseroth (Addgene viral prep # 100054-AAV1; http://addgene.org/100054; RRID: Addgene_100054)
pAAV-CAG-flex-ChR2-tdTomato	(Tang et al., 2016)	pAAV-CAG-FLEXFRT-ChR2(H134R)-mCherry was a gift from Connie Cepko (Addgene viral prep # 75470-AAV1; http://addgene.org/75470; RRID: Addgene_75470)
AAV-flex-Arch-GFP	(Chow et al., 2010)	AAV-FLEX-Arch-GFP was a gift from Edward Boyden (Addgene viral prep # 22222-AAV1;http://addgene.org/22222; RRID: Addgene_22222)
pACAGW-ChR2-Venus-AAV	(Petreanu et al., 2009)	pACAGW-ChR2-Venus-AAV was a gift from Karel Svoboda (Addgene viral prep # 20071-AAV1;http://addgene.org/20071; RRID: Addgene_20071)
pAAV-Ef1a-mCherry-IRES-Cre	(Fenno et al., 2014)	pAAV-Ef1a-mCherry-IRES-Cre was a gift from Karl Deisseroth (Addgene viral prep # 55632-AAVrg;http://addgene.org/55632; RRID: Addgene_55632)
pAAV-CAG-GFP	Unpublished data	pAAV-CAG-GFP was a gift from Edward Boyden (Addgene viral prep # 37825-AAVrg;http://addgene.org/37825; RRID: Addgene_37825)
pAAV-hSyn-mcherry	Unpublished data	pAAV-hSyn-mCherry was a gift from Karl Deisseroth (Addgene viral prep # 114472-AAVrg;http://addgene.org/114472; RRID: Addgene_114472)
pAAV-CAG-hChR2(H134R)-mCherry	(Mao et al., 2011)	AAV-CAG-hChR2-H134R-tdTomato was a gift from Karel Svoboda (Addgene viral prep # 28017-AAVrg; http://addgene.org/28017; RRID: Addgene_28017)
pENN-AAV-hSyn-Cre	Unpublished data	pENN.AAV.hSyn.Cre.WPRE.hGH was a gift from James M. Wilson (Addgene viral prep # 105553-AAV1; http://addgene.org/105553; RRID: Addgene_105553)
AAV-SYN-flex-PSAM4-GlyR-EGFP	(Magnus et al., 2019)	AAV SYN flex PSAM4 GlyR IRES EGFP was a gift from Scott Sternson (Addgene viral prep # 119741-AAV5; http://addgene.org/119741; RRID: Addgene_119741)
Chemicals, peptides, and recombinant proteins		
Fluoro-gold	Fluorochorme	Patent No. 4716905
VectaShield without DAPI	Vector Laboratories	RRID: AB_2336789
VectaShield with DAPI	Vector Laboratories	RRID: AB_2336790
Neurobiotin Tracer	Vector Laboratories	Catalog No. SP-1120
Experimental models: Organisms/strains		
Mouse/C57BL/6J	Jackson Lab	RRID: IMSR_JAX:000664
Mouse/CamKII-Cre	Jackson Lab	RRID: IMSR_JAX:005359
Software and algorithms		
MATLAB	MathWorks	https://www.mathworks.com/products/matlab.html?s_tid=hp_products_matlab
iPython and Jupyter	(Perez and Granger, 2007)	https://jupyter.org

REAGENT or RESOURCE	SOURCE	IDENTIFIER
Minitab Statistical Softeware	Minitab	https://www.minitab.com/en-us/products/minitab/
Fiji (ImageJ)	NIH	https://fiji.sc
Clustering code	This paper	https://github.com/wyomingneuron/Clustering